



SQuIGGLE: Studying Quenching in Intermediate- z Galaxies—Gas, Angular Momentum, and Evolution

Katherine A. Suess^{1,2,3} , Mariska Kriek^{1,4} , Rachel Bezanson⁵ , Jenny E. Greene⁶ , David Setton⁵ , Justin S. Spilker^{7,18} , Robert Feldmann⁸ , Andy D. Goulding⁶ , Benjamin D. Johnson⁹ , Joel Leja^{10,11,12} , Desika Narayanan^{13,14,15} , Khalil Hall-Hooper¹⁶ , Qiana Hunt¹⁷ , Sidney Lower¹³ , and Margaret Verrico⁵

¹ Astronomy Department, University of California, Berkeley, CA 94720, USA; suess@ucsc.edu

² Department of Astronomy and Astrophysics, University of California, Santa Cruz, 1156 High Street, Santa Cruz, CA 95064 USA

³ Kavli Institute for Particle Astrophysics and Cosmology and Department of Physics, Stanford University, Stanford, CA 94305, USA

⁴ Leiden Observatory, Leiden University, P.O.Box 9513, NL-2300 AA Leiden, The Netherlands

⁵ Department of Physics and Astronomy and PITT PACC, University of Pittsburgh, Pittsburgh, PA 15260, USA

⁶ Department of Astrophysical Sciences, Princeton University, Princeton, NJ 08544, USA

⁷ Department of Astronomy, University of Texas at Austin, 2515 Speedway, Stop C1400, Austin, TX 78712, USA

⁸ Institute for Computational Science, University of Zurich, CH-8057 Zurich, Switzerland

⁹ Center for Astrophysics | Harvard & Smithsonian, 60 Garden Street, Cambridge, MA 02138, USA

¹⁰ Department of Astronomy & Astrophysics, The Pennsylvania State University, University Park, PA 16802, USA

¹¹ Institute for Computational & Data Sciences, The Pennsylvania State University, University Park, PA 16802, USA

¹² Institute for Gravitation and the Cosmos, The Pennsylvania State University, University Park, PA 16802, USA

¹³ Department of Astronomy, University of Florida, 211 Bryant Space Science Center, Gainesville, FL 32611, USA

¹⁴ University of Florida Informatics Institute, 432 Newell Drive, CISE Bldg E251 Gainesville, FL 32611, US

¹⁵ Cosmic Dawn Centre at the Niels Bohr Institute, University of Copenhagen and DTU-Space, Technical University of Denmark, Denmark

¹⁶ Department of Mathematics, North Carolina State University, 2108 SAS Hall Box 8205, Raleigh, NC 27695, USA

¹⁷ Department of Astronomy, University of Michigan, 1085 S University, Ann Arbor, MI 48109, USA

Received 2021 June 23; revised 2021 November 23; accepted 2021 November 23; published 2022 February 16

Abstract

We describe the Studying Quenching in Intermediate- z Galaxies: Gas, angular momentum, and Evolution (SQuIGGLE) survey of intermediate-redshift post-starburst galaxies. We leverage the large sky coverage of the Sloan Digital Sky Survey to select ~ 1300 recently quenched galaxies at $0.5 < z \leq 0.9$ based on their unique spectral shapes. These bright, intermediate-redshift galaxies are ideal laboratories to study the physics responsible for the rapid quenching of star formation: they are distant enough to be useful analogs for high-redshift quenching galaxies, but low enough redshift that multiwavelength follow-up observations are feasible with modest telescope investments. We use the `Prospector` code to infer the stellar population properties and nonparametric star formation histories (SFHs) of all galaxies in the sample. We find that SQuIGGLE galaxies are both very massive ($M_* \sim 10^{11.25} M_\odot$) and quenched, with inferred star formation rates $\lesssim 1 M_\odot \text{ yr}^{-1}$, more than an order of magnitude below the star-forming main sequence. The best-fit SFHs confirm that these galaxies recently quenched a major burst of star formation: $>75\%$ of SQuIGGLE galaxies formed at least a quarter of their total stellar mass in the recent burst, which ended just ~ 200 Myr before observation. We find that SQuIGGLE galaxies are on average younger and more burst-dominated than most other $z \lesssim 1$ post-starburst galaxy samples. This large sample of bright post-starburst galaxies at intermediate redshift opens a wide range of studies into the quenching process. In particular, the full SQuIGGLE survey will investigate the molecular gas reservoirs, morphologies, kinematics, resolved stellar populations, active galactic nucleus incidence, and infrared properties of this unique sample of galaxies in order to place definitive constraints on the quenching process.

Unified Astronomy Thesaurus concepts: Post-starburst galaxies (2176); Galaxy quenching (2040); Quenched galaxies (2016); Galaxy evolution (594); Galaxy ages (576)

Supporting material: machine-readable tables

1. Introduction

For nearly a century, astronomers have divided galaxies into two distinct categories based on their morphologies: spirals and ellipticals (Hubble 1926). This “galaxy bimodality” has since been shown to extend to myriad other properties, including color, size, environment, molecular gas content, and star

formation rate (SFR; e.g., Blanton et al. 2003; Kauffmann et al. 2003; Shen et al. 2003; Noeske et al. 2007; Wuyts et al. 2011). Star-forming galaxies tend to be large, blue, rotationally supported, and gas-rich; in contrast, quiescent galaxies are red, smaller at fixed mass, supported by random motions, and gas poor. However, the fundamental question of *why* this galaxy bimodality exists remains unanswered to the present day. What physical processes are responsible for “quenching” star formation in galaxies? And why does a cessation of star formation appear to go hand-in-hand with structural and kinematic changes?

A variety of theoretical mechanisms have been proposed to form massive compact quiescent galaxies. These proposed

¹⁸ NHFP Hubble Fellow.



mechanisms range from intense centrally concentrated starbursts triggered by gas-rich major mergers (e.g., Hopkins et al. 2008; Wellons et al. 2015), to very early assembly in a much denser universe (e.g., Naab et al. 2009; Wellons et al. 2015), to “morphological” quenching, where the transition from disk to spheroid stabilizes gas reservoirs (e.g., Martig et al. 2009). While all of these mechanisms could shut down star formation by depleting, removing, heating, or stabilizing molecular gas reservoirs, the resulting quenched galaxies differ in key observables including age gradients, rotational support, and morphology. Detailed multiwavelength follow-up of quenched galaxies holds the key to distinguishing between these theoretical quenching mechanisms. This multiwavelength follow-up is most effective when performed in galaxies that have *just* concluded their major star-forming phase: the signatures of the quenching mechanism should still be apparent, and not diluted by later mergers or secular evolution. The question then becomes how to identify these recently quenched galaxies.

Growing observational evidence suggests that there are at least two distinct pathways to quenching: galaxies can quench rapidly through the post-starburst phase, or quench slowly through the green valley phase (e.g., Barro et al. 2013; Faber & Pérez-González et al. 2014; Schawinski et al. 2014; Wild et al. 2016; Carnall et al. 2018; Forrest et al. 2018; Rowlands et al. 2018; Wu et al. 2018; Belli et al. 2019; Suess et al. 2021). In this paper, we focus on the rapid quenching mode. These fast-quenching post-starburst galaxies, sometimes also called “K+A” or “E+A” galaxies, experienced a recent burst of intense star formation that concluded within the past \sim gigayear (e.g., Dressler & Gunn 1983; Couch & Sharples 1987; see French 2021 for a recent review). Observationally, these galaxies are characterized by spectra that are dominated by A-type stars: the burst finished long enough ago that the most massive stars have died, but recently enough that the slightly longer-lived and less massive stars are still alive to dominate the optical spectrum. These spectra typically show strong Balmer breaks, deep Balmer absorption lines, weak or absent nebular emission lines, and blue slopes redward of the Balmer break.

A variety of observational techniques have been used to select post-starburst galaxies over a wide redshift range. “E+A” or “K+A” post-starburst galaxies in the local universe are often selected by their high H δ equivalent widths and low [OII] luminosities; in combination, these spectral features indicate significant recent star formation but little ongoing star formation (e.g., Zabludoff et al. 1996; Dressler et al. 1999; Goto 2005; Brown et al. 2009; French et al. 2015). Some works use spectral template fitting approaches, which can identify galaxies whose light is dominated by young stars (e.g., Quintero et al. 2004; Pattarakijwanich et al. 2016). An alternate technique pioneered by Wild et al. (2014) uses principal component analysis (PCA), which effectively selects for the unique spectral shape of post-starburst galaxies (see also, e.g., Almaini et al. 2017; Maltby et al. 2018). A similar spectral shape identification approach was also used by Kriek et al. (2010), using synthetic rest-frame colors instead of PCA-based “supercolors.” Finally, some studies have selected post-starburst galaxies based on their location in the *UVJ* plane (e.g., Whitaker et al. 2012a; Belli et al. 2019; Suess et al. 2020; see also Akins et al. 2021). These different methods of selecting post-starburst galaxies produce samples that are

relatively similar, but do not fully overlap; we will explore the differences in these sample selection methods in more detail later in this paper.

While massive post-starburst galaxies are relatively rare across cosmic time (making up $\lesssim 5\%$ of the total $M_* > 10^{10} M_\odot$ population at $z \leq 2.2$; Wild et al. 2016), their number density evolves rapidly with redshift. At $z \sim 2$, post-starburst galaxies are common enough to explain half of the total growth in the red sequence; by $z \sim 1.4$, they represent just $\sim 20\%$ of all transitioning galaxies (Belli et al. 2019). By $z \sim 0$, massive post-starburst galaxies are so rare that they contribute negligibly to the growth of the quiescent population (Rowlands et al. 2018). These results imply that, while post-starburst galaxies play an important role in quenching at cosmic noon, their importance to the overall landscape of galaxy transformation diminishes toward lower redshifts.

The nature of post-starburst galaxies may also differ between $z \sim 0$ and $z \sim 1$. Higher-redshift post-starburst galaxies generally appear to be more burst-dominated than their low-redshift counterparts: simple modeling of H δ and D_n4000 values indicates that $z \sim 0$ post-starburst galaxies formed just 5%–10% of their mass in the recent burst, whereas $z > 0.5$ post-starburst galaxies appear to have formed the majority of their mass in the recent burst (Suess et al. 2017). Full spectral modeling of post-starburst star formation histories (SFHs) confirms these findings: the median burst mass fraction of $z \sim 0$ post-starburst galaxies is $\sim 10\%$ (French et al. 2018), in contrast to the $\sim 70\%$ median burst mass fractions of $z \sim 1$ post-starburst galaxies (Wild et al. 2020). Low-redshift post-starburst galaxies also tend to be less massive than their higher-redshift counterparts (e.g., Wild et al. 2016; Rowlands et al. 2018), although they are not so low-mass that environmental effects play significant roles in their quenching (e.g., Zabludoff et al. 1996; Feldmann et al. 2011). Taken together, these results indicate that high-redshift post-starburst galaxies are in the process of rapidly quenching their *primary* epoch of star formation, whereas low-redshift post-starburst galaxies are rapidly shutting down a smaller burst of late-time star formation that does not contribute as significantly to their stellar mass.

This redshift dependence complicates observational studies of quenching: pinpointing the physics responsible for shutting down the bulk of star formation requires looking beyond the local universe, but detailed follow-up observations require significant (and potentially prohibitive) telescope investments at $z \gtrsim 1$. Even spectroscopic confirmation of post-starburst galaxies is difficult at $z > 1$, with samples consisting of a few tens of galaxies (e.g., Bezanson et al. 2013; Maltby et al. 2016; Wild et al. 2020) as opposed to the hundreds or thousands of $z \lesssim 0.1$ post-starburst galaxies that can be identified from large all-sky surveys (e.g., Dressler et al. 1999; Quintero et al. 2004; Goto 2005; Brown et al. 2009; French et al. 2015; Alatalo et al. 2016).

Our goal in this paper is to bridge the gap between these low- and high-redshift samples by selecting bright *intermediate-redshift* post-starburst galaxies at $0.5 < z \lesssim 1$ that will serve as the ideal testbeds to understand the physics of quenching. We aim to find a large sample of galaxies that have high burst mass fractions and are therefore in the process of shutting down their major epoch of star formation. At the same time, we want these galaxies to be bright enough to conduct full multiwavelength follow-up studies with reasonable telescope investments. These

bright, massive, intermediate-redshift post-starburst galaxies will not provide us with a complete census of how star formation shuts down across all stellar masses and timescales; however, they will serve as excellent laboratories to study how rapid quenching proceeds in massive galaxies. This sample selection is now possible due to the Sloan Digital Sky Survey (SDSS), which provides millions of spectra over our targeted redshift range. This enormous public database allows us to identify a statistically large sample of rare, bright, young post-starburst systems. With this sample, we will be Studying Quenching in Intermediate- z Galaxies: Gas, angular momentum, and Evolution (SQUIGGLE). The SQUIGGLE sample will serve as the ideal testbed to study the quenching process in massive galaxies in detail.

This paper is organized as follows. In Section 2, we describe our post-starburst sample selection. We also generate mock galaxy spectra with known properties, and use those mocks to investigate what types of galaxies are included in our sample selection. In Section 3, we use the `Prospector` Bayesian stellar population synthesis code to fit the stellar masses, dust properties, and SFHs of the galaxies in our sample. In particular, we use these derived SFHs to investigate how long SQUIGGLE post-starburst galaxies have been quiescent, the fraction of their mass that was formed in a recent starburst, and their ongoing SFRs. In Section 4, we calculate SFRs from spectral lines present in the SDSS spectra of our galaxies, and compare these results to the `Prospector` SFRs. In Section 5, we place the SQUIGGLE sample in context by comparing it to other post-starburst samples. Finally, in Section 6 we briefly describe the science objectives of the remainder of the SQUIGGLE survey. Throughout this paper we assume a flat Λ cold dark matter cosmology with $\Omega_m = 0.3$, $\Omega_\Lambda = 0.7$, and $h = 0.7$. We also assume a Chabrier (2003) initial mass function (IMF).

2. Sample Selection

In this section, we describe how we select post-starburst galaxies from the SDSS. Our selection is designed to select the brightest, most massive, most burst-dominated post-starburst galaxies at $z \sim 0.7$, with the goal of identifying galaxies that are ideal targets for multiwavelength follow-up studies of the quenching process. We explore the differences between our sample selection algorithm and those used in previous studies in Section 5.

For the SQUIGGLE sample, we follow the Kriek et al. (2010) method and select post-starburst galaxies from the SDSS based on their unique spectral shapes. Synthetic medium-band rest-frame U_m , V_m , and B_m filters are designed to target both the Balmer break and the slope of the spectrum redward of the break; as shown in Figure 1, these two rest-frame colors alone are effective at selecting post-starburst galaxies. Model spectra (generated with the Flexible Stellar Population Synthesis, FSPS; Conroy et al. 2009; Conroy & Gunn 2010) of a post-starburst galaxy (black), a fully quiescent galaxy (red), an unobscured star-forming galaxy (blue), and a dusty star-forming galaxy (purple) are shown over the same wavelength range. The bottom-left panel in Figure 1 shows the location of these four spectra in UBV space, as well as the density of all SDSS spectra with $z > 0.5$. Our post-starburst color selection cuts, described in detail below, are shown with black lines. The color cuts include the post-starburst galaxy while excluding both star-forming and older quiescent galaxies;

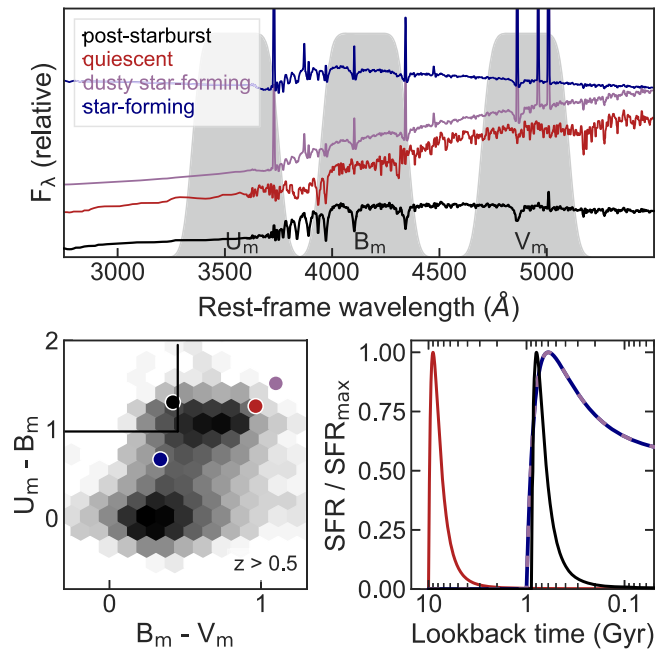


Figure 1. Demonstration of color-based selection technique. Top: gray shaded regions show the synthetic rest-frame U_m , B_m , and V_m filters. Blue, purple, red, and black curves show example synthetic spectra of an unobscured star-forming galaxy, a dusty star-forming galaxy, a quiescent galaxy, and a post-starburst galaxy; spectra have an arbitrary factor added to F_λ for visibility. Bottom left: $U_m - B_m$ as a function of $B_m - V_m$; the shaded background represents the relative density of all $z > 0.5$ galaxies in the SDSS, while the black, blue, purple, and red points show the colors of the spectra shown in the top plot. The black lines show our color criteria for a galaxy to be selected as post-starburst. Post-starburst galaxies can be distinguished from other galaxy types in this color-color space: the $U_m - B_m$ color separates post-starburst galaxies from unobscured star-forming galaxies, while the $B_m - V_m$ color separates post-starburst galaxies from dusty star-forming galaxies and older quiescent galaxies. Bottom right: SFHs of the four synthetic spectra shown in the top plot. The post-starburst galaxy (black) clearly has a different SFH than either the quiescent galaxy, which formed its stars much earlier, or the two star-forming galaxies, which have significant ongoing star formation.

just $\sim 5\%$ of all $z > 0.5$ galaxies in the SDSS satisfy these color cuts. Figure 1 shows that unobscured star-forming galaxies—including galaxies that may have ongoing starbursts—have similar $B_m - V_m$ colors to post-starburst galaxies, but weaker Balmer breaks that do not satisfy our $U_m - B_m$ cut. In contrast, both dusty star-forming galaxies, and older quiescent galaxies have similar $U_m - B_m$ colors as post-starburst galaxies, but redder $B_m - V_m$ colors. Spectrally, older quiescent galaxies and post-starburst galaxies can be distinguished by the differences in the strength of the Balmer break, the slope of the spectrum redward of the break, and the depth of both the Balmer absorption lines and the calcium H and K lines. Dusty star-forming galaxies differ from post-starburst galaxies mainly in the slope of the spectrum redward of the Balmer break and the strength of the nebular emission lines.

Our parent sample consists of all 1,921,000 galaxies in the SDSS DR14 spectroscopic catalog (Abolfathi et al. 2018) with $z > 0.5$. We then make a quality cut that removes nonphysical spectra: we calculate the $r - i$ and $i - z$ colors from the SDSS spectrum, and remove any galaxies for which these spectral colors differ from the SDSS photometric colors by more than 0.25 dex. We note that at these redshifts, the fiber encompasses $\gtrsim 75\%$ of the total light from these compact post-starburst galaxies; typically the spectral and photometric colors are within 0.05 dex. We ensure that the wavelength

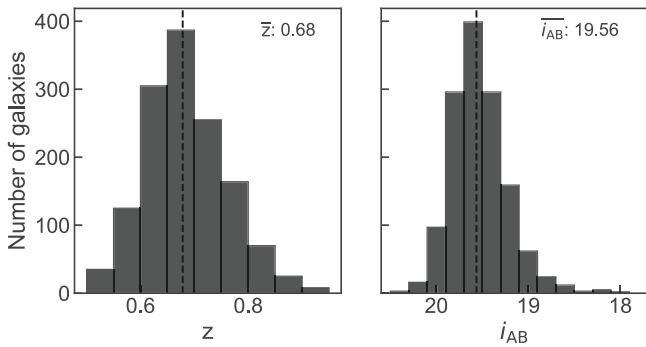


Figure 2. Histograms of the redshift and i -band magnitude of all SQuIGGLE galaxies.

range of the SDSS spectrum covers our rest-frame U_m , B_m , and V_m filters, and then we calculate the flux in each synthetic rest-frame filter. To ensure high-quality spectra, we require a signal-to-noise ratio (S/N) ≥ 6 in both our B_m and V_m filters; this S/N cutoff was chosen by examining representative spectra by eye. We do not require a minimum S/N in the U_m filter, because post-starburst galaxies typically have minimal UV flux and thus low S/N blueward of the Balmer break (see, e.g., Figure 1). After these initial quality cuts, 32,168 galaxies remain in the parent sample. Finally, we select all objects in this sample with $U - B > 0.975$ and $-0.25 < B - V < 0.45$ as post-starburst galaxies. Our final sample includes 1318 unique post-starburst galaxies. These galaxies form the full SQuIGGLE sample.

Figure 2 shows histograms of the redshift and i -band magnitude distribution of the full SQuIGGLE sample. By construction, all galaxies have $z \geq 0.5$. The median sample redshift is $z = 0.68$, with a tail of galaxies up to $z = 0.94$. This redshift distribution is effectively a competition between apparent magnitude (there are fewer high- S/N SDSS spectra at higher redshift) and the number density evolution of post-starburst galaxies (there are many more post-starburst galaxies at higher redshift; e.g., Wild et al. 2016; Belli et al. 2019). The i -band magnitudes of SQuIGGLE galaxies range from 17.9 to 20.5, with the faint-end cutoff primarily driven by our S/N cut.

Figure 3 shows a stacked spectrum of all 1318 post-starburst galaxies in SQuIGGLE, normalized using the flux between 4150 and 4250 Å. The gray shaded region shows the 16th–84th percentile of all spectra. This stacked spectrum clearly shows the representative characteristics of a post-starburst galaxy: a strong Balmer break, deep Balmer absorption lines, and weak [O II] emission. Spectral modeling (Section 3) indicates that 98% of SQuIGGLE galaxies have SFRs below the main sequence, and 95% of SQuIGGLE galaxies formed $>10\%$ of their stellar mass in a recent burst; this indicates that our sample selection technique is very effective at identifying recently quenched galaxies.

We also measure the $H\delta$ equivalent width and the D_n4000 index for all galaxies in our sample. $H\delta$ traces recent star formation, while D_n4000 probes the age of the stellar population; together, these indices provide a fairly reliable indication of the galaxy’s evolutionary stage. We use the `pyphot` python package to calculate $H\delta_A$, and obtain error bars via bootstrap resampling. We measure D_n4000 from the SDSS spectra using the bandpass definitions from Balogh et al. (1999). In Figure 4, we show $H\delta_A$ as a function of D_n4000 for all galaxies in our sample (black points). To help place SQuIGGLE galaxies in context, Figure 4 also shows star-

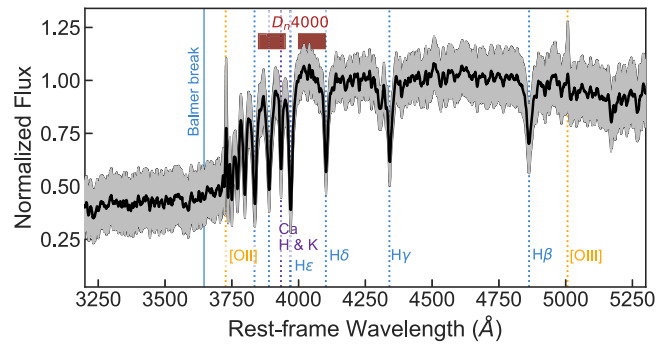


Figure 3. Stack of all post-starburst galaxies in the SQuIGGLE sample. The black line shows the median stacked spectrum; the gray shaded region indicates the 16th–84th percentile range of all spectra. SQuIGGLE galaxies have strong Balmer breaks, blue slopes redward of the break, deep Balmer absorption lines, and typically weak or absent [O II] and [O III] emission lines.

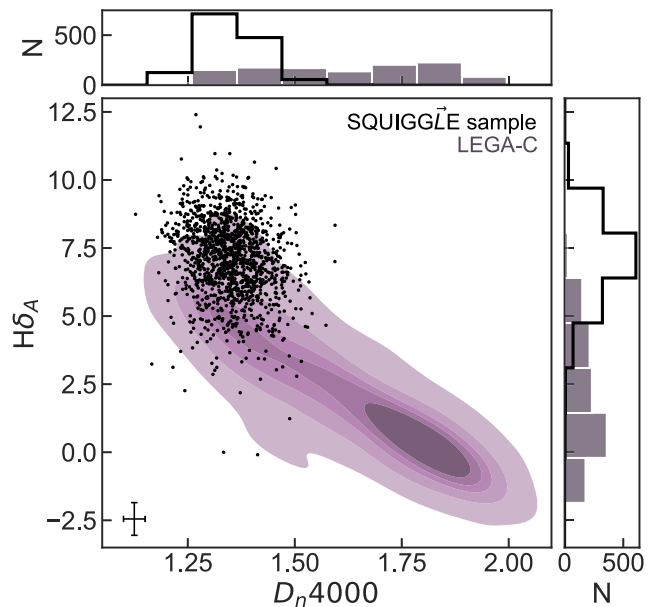


Figure 4. $H\delta_A$ as a function of D_n4000 for all SQuIGGLE galaxies (black points). A characteristic error bar for SQuIGGLE galaxies is shown in the lower left. Age increases toward the lower right of the diagram. The distribution of galaxies with similar stellar mass and redshift from the LEGA-C survey is shown by the shaded purple background. Our selection has clearly resulted in a sample of galaxies with high $H\delta$ equivalent widths and low D_n4000 indices, despite not explicitly selecting on these parameters.

forming and quiescent galaxies from the Large Early Galaxy Census (LEGA-C) spectroscopic survey (van der Wel et al. 2016) with $0.5 \leq z \leq 1$ and $\log M_*/M_\odot \geq 10.7$. These mass and redshift ranges roughly match those of SQuIGGLE, though LEGA-C’s relatively small area means that it lacks the highest stellar masses found in SQuIGGLE.

Despite the fact that we do not explicitly select post-starburst galaxies using either of these two indices (unlike some post-starburst galaxy selection techniques, which use an $H\delta_A$ cut), we see that SQuIGGLE galaxies are clustered at high $H\delta_A$ and low D_n4000 . This result confirms that the galaxies in the SQuIGGLE sample are indeed fairly young. We again see that SQuIGGLE galaxies lie in a relatively extreme region of parameter space compared to the overall galaxy population. These extreme $H\delta_A$ and D_n4000 values hint at the fact that SQuIGGLE galaxies have distinct SFHs from the majority of

Table 1
Basic Properties of SQuIGGLE Post-starburst Galaxies

SDSS ID	R.A. (deg)	Decl. (deg)	z_{spec}	$H\delta_A$ (Å)	D_n4000	σ_* (km s ⁻¹) ^a	Aperture Correction
spec-6137-56270-0195	353.79039	16.10073	0.7473	7.86 ± 0.51	1.21 ± 0.02	186 ± 52	1.50
spec-0978-52431-0077	260.01290	30.28743	0.6840	9.45 ± 0.33	1.25 ± 0.01	223 ± 42	1.07
spec-5192-56066-0419	238.72249	38.33752	0.7237	7.49 ± 0.62	1.41 ± 0.03	222 ± 123	1.21
spec-5288-55865-0858	132.07321	13.07628	0.5233	8.53 ± 0.47	1.29 ± 0.02	211 ± 53	0.95
spec-4575-55590-0605	144.35677	36.50522	0.6206	8.11 ± 0.43	1.40 ± 0.02	167 ± 20	1.39
spec-3817-55277-0279	135.90519	3.81953	0.7570	4.54 ± 0.50	1.45 ± 0.02	261 ± 46	1.47
spec-5140-55836-0177	21.74532	14.35716	0.6946	7.87 ± 0.53	1.36 ± 0.02	164 ± 43	1.35
spec-1630-54476-0502	53.22548	-6.20368	0.5715	5.02 ± 0.39	1.40 ± 0.02	239 ± 33	1.29
spec-3754-55488-0041	120.22957	32.94343	0.7037	5.26 ± 0.65	1.51 ± 0.03	265 ± 62	1.64
spec-6649-56364-0311	166.58688	45.04543	0.6391	6.53 ± 0.59	1.42 ± 0.03	191 ± 35	1.72
spec-5048-56218-0165	337.14303	10.75239	0.6671	7.82 ± 0.71	1.40 ± 0.03	129 ± 65	1.57
spec-6054-56089-0547	225.25613	42.77234	0.6094	5.58 ± 0.39	1.40 ± 0.02	234 ± 28	1.45
spec-4403-55536-0765	27.85715	6.27124	0.6698	5.28 ± 0.64	1.31 ± 0.02	232 ± 50	1.72
spec-6032-56067-0159	236.68717	45.81196	0.6819	8.75 ± 0.63	1.33 ± 0.03	205 ± 64	1.26
spec-6639-56385-0597	177.92877	43.34649	0.7691	7.64 ± 0.73	1.36 ± 0.02	229 ± 47	1.58
spec-4013-55629-0073	228.42489	2.08515	0.7409	5.92 ± 0.52	1.39 ± 0.02	146 ± 40	1.48
spec-5993-56070-0251	199.47152	22.03277	0.7208	7.73 ± 0.44	1.31 ± 0.02	218 ± 57	1.68
spec-5014-55717-0745	257.42214	27.66418	0.6926	8.97 ± 0.69	1.46 ± 0.03	175 ± 52	1.35
spec-5291-55947-0601	132.52735	11.19210	0.6111	6.98 ± 0.57	1.25 ± 0.02	288 ± 21	1.35
spec-5475-56011-0379	222.19133	10.16960	0.6462	7.28 ± 0.34	1.32 ± 0.01	209 ± 30	1.71
...

Note.

^a From the Penalized Pixel-Fitting (pPXF) fits described in Greene et al. (2020).

(This table is available in its entirety in machine-readable form.)

galaxies at similar redshifts and stellar masses; we will explore this in greater detail in Section 3.

Table 1 lists the basic properties of the post-starburst galaxies identified by SQuIGGLE.

2.1. Why Were These Galaxies Targeted by SDSS?

Here, we examine the target flags of the selected SQuIGGLE galaxies to understand why they were included in the SDSS spectroscopic sample. The vast majority of SQuIGGLE galaxies—1132 out of 1318, $\sim 82\%$ —are part of the main constant mass (“CMASS”) Baryon Oscillation Spectroscopic Survey (BOSS) sample (Dawson et al. 2013). The CMASS selection used color–magnitude cuts designed to target massive galaxies at $0.4 < z < 0.7$. An additional 11 galaxies are part of the sparse CMASS sample, which includes fainter and bluer galaxies than the main CMASS sample. Sixty-four galaxies are part of the “commissioning” CMASS sample, which used slightly different color cuts than the final CMASS survey. The remaining 111 post-starburst galaxies were targeted as part of 24 different programs within SDSS. The majority of these 111 galaxies were selected as BOSS ancillary targets because their *ugriz* or Wide-field Infrared Survey Explorer (WISE) colors resembled those of high-redshift quasars or luminous red galaxies. Several others were selected because they had matches in the Chandra Source Catalog (Evans et al. 2010) or the Faint Images of the Radio Sky at 20-cmTimeters radio survey (FIRST; Becker et al. 1995, see also Greene et al. 2020). Galaxies with non-CMASS target flags tend to be slightly brighter and lie at lower redshifts than the median of the full SQuIGGLE sample.

2.2. Understanding Our Sample Selection: How Do Physical Parameters Map onto $U_m - B_m$ and $B_m - V_m$ Colors?

In order to understand the types of galaxies that fall into our color-based selection method, we generate a set of mock SDSS-like spectra then map their physical properties onto UB V color space. We generate these mock galaxy spectra using FSPS (Conroy et al. 2009; Conroy & Gunn 2010) assuming a Chabrier (2003) IMF, the Calzetti et al. (2000) dust law, a total stellar mass of $10^{11.25} M_\odot$, and a velocity dispersion of 200 km s^{-1} . We vary the dust attenuation ($0 \leq A_v/\text{mag} \leq 2.5$), the metallicity ($0 \leq \log Z/Z_\odot \leq 0.5$), and the spectral S/N (10%–90% noise levels of our observed SQuIGGLE spectra). We model the SFHs of the mock galaxies as a delayed τ component plus a recent top-hat burst; we vary the mass fraction in the recent burst ($10\% \leq f_{\text{burst}} \leq 99\%$), the duration of the recent burst ($100 \leq t_{\text{burst}}/\text{Myr} \leq 600$), the time since quenching ($0.05 \leq t_q/\text{Gyr} \leq 1.0$), and the SFR after quenching (e.g., the amount of “frosting”, $10^{-5} \leq \text{SFR}_q/M_\odot \text{ yr}^{-1} \leq 30$). We explain the generation of these mock spectra in more detail in a forthcoming paper, Suess et al. (2021, in preparation), which examines the best methods to recover accurate SFHs for post-starburst galaxies.

We generate 5000 mock galaxy spectra, then run our color-based selection algorithm (Section 2) on the set of mock spectra. 1821 of the 5000 mock galaxies are classified as post-starburst by our sample selection criteria. Figure 5 shows $U_m - B_m$ versus $B_m - V_m$ for all 5000 mock spectra. Each panel is colored by a different physical parameter, and our post-starburst color cuts are shown by the solid black lines. While f_{burst} , t_q , A_v , and SFR_q show clear gradients across UB V space, neither metallicity nor the length of the recent burst exhibit coherent trends. This indicates that our sample selection does

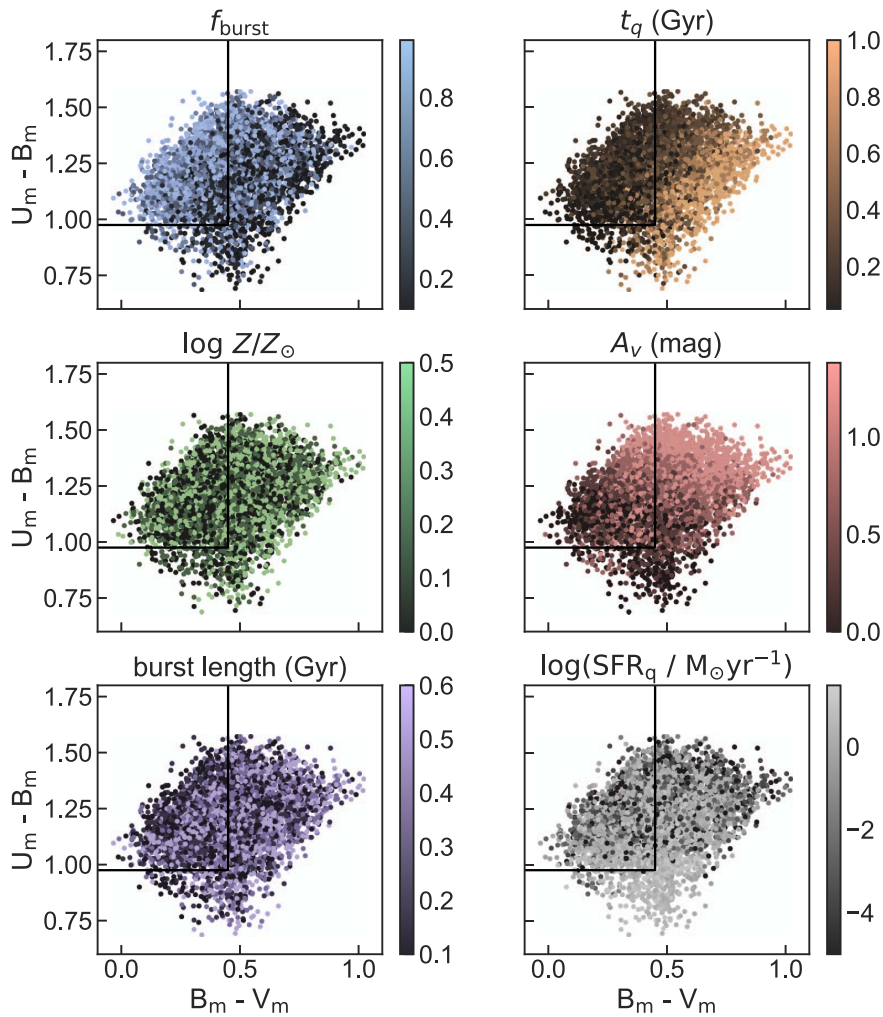


Figure 5. $U_m - B_m$ vs. $B_m - V_m$ colors for 5000 synthetic spectra generated with FSPS. The black lines show our color-based post-starburst galaxy sample selection. Each panel is colored by one of the parameters we vary to create the grid of synthetic spectra. $U_m - B_m$ and $B_m - V_m$ are sensitive to changes in burst mass fraction, time since quenching, dust extinction, and current SFR; however, the colors are not sensitive to metallicity or the timescale of the older burst of star formation. Galaxies that fall into our post-starburst galaxy selection tend to have high f_{burst} , low t_q , low A_v , and relatively low SFR.

not prefer galaxies of a specific t_{burst} or metallicity. However, the galaxies that we select as post-starburst tend to have high f_{burst} , low t_q , and relatively low A_v and SFR_q . This indicates that our sample selection algorithm is sensitive to relatively dust-free galaxies that recently quenched after a large starburst—exactly the types of galaxies we were attempting to target.

We also briefly explore correlations between these parameters. Figure 6 shows time since quenching as a function of burst mass fraction for the mock galaxies which are classified as post-starburst by our selection algorithm. The blue contours show relatively dust-free mock post-starburst galaxies, and the red contours show the dusty mock post-starburst galaxies. Relatively dust-free post-starburst galaxies can be found at a range of t_q and f_{burst} values. However, dusty galaxies are only classified as post-starburst if they quenched very recently, within the past ~ 200 Myr. We can therefore expect that, while the majority of galaxies in the SQuGGLE sample are likely not highly dust-obscured, some especially young dusty galaxies may be included in the sample. We do not find a significant difference in the t_q and f_{burst} values of low- and high-SFR mock post-starburst galaxies.

3. Extracting Star Formation Histories via Spectral Energy Distribution Fitting

In this section, we use the `Prospector` stellar population synthesis fitting code (Johnson & Leja 2017; Leja et al. 2017; Johnson et al. 2021) to investigate the stellar masses, dust properties, metallicities, SFRs, and SFHs of galaxies in the SQuGGLE sample.

Robust SFHs provide a wealth of information, allowing us to investigate how long these galaxies have been quenched (t_q), the fraction of their mass that was formed in the recent burst (f_{burst}), and the timescale of both the recent burst and the quenching process. However, traditional “parametric” SFH models that depend on just a few parameters impose strong priors on specific star formation rates (sSFRs) and mass-weighted ages, and results from these parametric fits may not accurately reflect the true mass assembly histories of galaxies (e.g., Carnall et al. 2019). Previous studies have worked to mitigate these biases by modeling post-starburst SFHs as the sum of two parametric components, one for the recent burst and one for the older stellar population (e.g., Kaviraj et al. 2007; French et al. 2018; Wild et al. 2020). While this approach improves on traditional

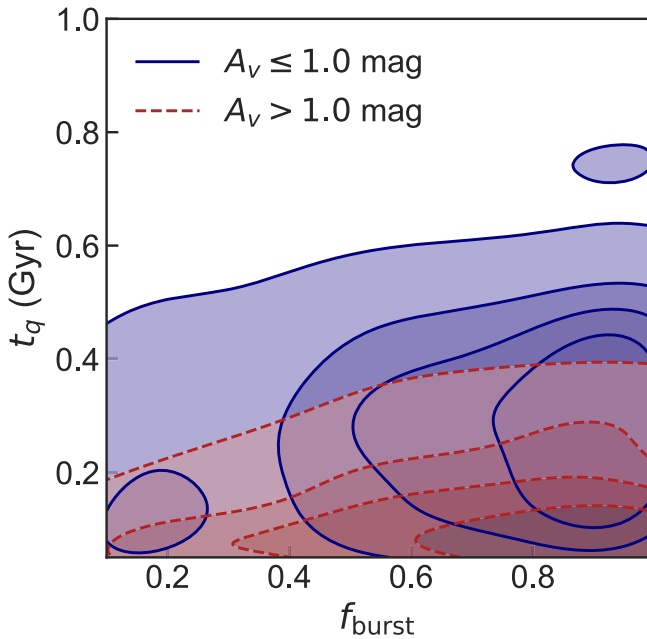


Figure 6. Time since quenching as a function of burst mass fraction for mock post-starburst galaxies that fall within our selection, split into more dusty (red, $A_v > 1.0$ mag) and less obscured (blue, $A_v \lesssim 1.0$ mag) galaxies. Our sample tends to select post-starburst galaxies with relatively high f_{burst} and low t_q . Dusty galaxies only fall in our sample if they quenched very recently.

parametric approaches by allowing the mass fraction in the recent burst to vary, it still explicitly imposes a specific shape for the recent burst and may thus bias results. Here, we use a “nonparametric” form for the SFH, which allows for arbitrary SFR in adjacent time bins. This approach introduces a larger number of free parameters into the fit in exchange for allowing more flexibility and freedom in the derived SFH. These nonparametric SFHs have been shown to more accurately recover galaxy properties such as stellar mass (e.g., Lower et al. 2020). Here, we develop and use a nonparametric model specifically tuned to recover the SFHs of post-starburst galaxies. With these fits, we allow for full flexibility in the burst shape, burst duration, burst mass fraction, and quenching timescale of SQuIGGLE post-starburst galaxies.

3.1. SED Fitting Setup

We fit the spectral energy distributions (SEDs) of all SQuIGGLE galaxies using the *Prospector* stellar population synthesis fitting software (Johnson & Leja 2017; Leja et al. 2017; Johnson et al. 2021). We use the *dynesty* dynamic nested sampling package (Speagle 2020), the FSPS stellar population synthesis models (Conroy et al. 2009; Conroy & Gunn 2010), the MILES spectral library (Sánchez-Blázquez et al. 2006; Falcón-Barroso et al. 2011), and the MIST isochrones (Choi et al. 2016; Dotter 2016; based on MESA, Paxton et al. 2011, 2013, 2015). We assume the Chabrier (2003) IMF, fix the model redshift to the SDSS spectroscopic redshift, and add nebular emission to the spectra using the default fixed parameters in *Prospector* (see Byler et al. 2017). We fit for stellar mass and metallicity using the mass-metallicity prior described in Leja et al. (2019b). We also fit for the velocity dispersion of the SDSS spectra, using a Gaussian prior with the mean and σ of the output pPXF (Cappellari 2017) velocity dispersion fits (see Greene et al. 2020). We assume the

Kriek & Conroy (2013) dust law, with a free A_v and dust index; in this dust law, the bump strength is tied to the slope. Following, e.g., Wild et al. (2020), we assume that the attenuation is doubled around young ($< 10^7$ yr) stars. We fix the shape of the IR SED following the Draine & Li (2007) dust emission templates, with $U_{\text{min}} = 1.0$, $\gamma_e = 0.01$, and $q_{\text{PAH}} = 2.0$. We also include both a spectroscopic jitter term and the *Prospector* pixel outlier model, which are designed to prevent misestimated spectroscopic uncertainties or bad spectral pixels from skewing the output.

Our adopted SFH is a modified version of the flexible continuity prior from Leja et al. (2019a), and is illustrated in Figure 7. The SFH includes three fixed-edge time bins at the beginning of the universe, five flexible-edge time bins covering the 2 Gyr before observation, and a final bin where we fit for both the bin length and the SFR. All five of the flexible-edge bins form an equal stellar mass, and the edges of the flexible bins are adjusted at each likelihood call based on the $\log(\text{SFR})$ ratio between adjacent bins; this parameterization is described in detail in Leja et al. (2019b). The SFH thus has nine free parameters: eight $\log(\text{SFR})$ ratios, plus the width of the final time bin. Following Leja et al. (2019b), we place Student- t priors on the $\log(\text{SFR})$ ratio between adjacent time bins. We center the priors such that they follow the predicted SFH for a massive quiescent galaxy at a similar redshift from Universe-Machine (Behroozi et al. 2019). This prior is more physically motivated than a prior centered at zero, which would imply that galaxies form stars at a constant rate across time. A forthcoming paper, Suess et al. (2021, in preparation), describes this SFH model in more detail and presents mock recovery tests and comparisons with multiple other SFH parameterizations. The SFH we use here was designed to use a relatively small number of parameters to capture both a recent burst of arbitrary mass fraction and length, a variable quenching timescale, and a variable amount of residual star formation after the burst ends. Suess et al. (2021, in preparation) shows that for SQuIGGLE-like galaxies, this fitting methodology recovers t_q with just 0.06 dex of scatter and f_{burst} with 0.12 dex of scatter.

We define a “burst” for each galaxy based on the output SFH. We interpolate the SFH to a uniform 1 Myr timescale, then define the burst start and end as the time when the time derivative of the SFH rises above and drops below a threshold value. This threshold is the same for all galaxies in the sample, and was tuned by visual examination of representative SFHs. In addition to basic quantities such as stellar mass and A_v , we also report several quantities derived from this burst. We define t_q as the time when the recent starburst ended based on our SFH derivative threshold; this quantity tells us how long the galaxy has been quenched. We also define m_{burst} to be the stellar mass formed in the burst, and f_{burst} to be the fraction of the total stellar mass formed during the burst. Suess et al. (2021, in preparation) describes these definitions in more detail, and explores several alternate definitions of t_q including the sSFR-based definitions used by Tacchella et al. (2021). While the exact numerical value of t_q depends on the definition used, in general different definitions produce quantitatively similar results.

3.1.1. Data Included in the SED Fits

We fit the *Prospector* model described above jointly to both photometry and spectroscopy. We include the SDSS ugriz photometry and the WISE 3.4 and 4.6 μm photometric points.

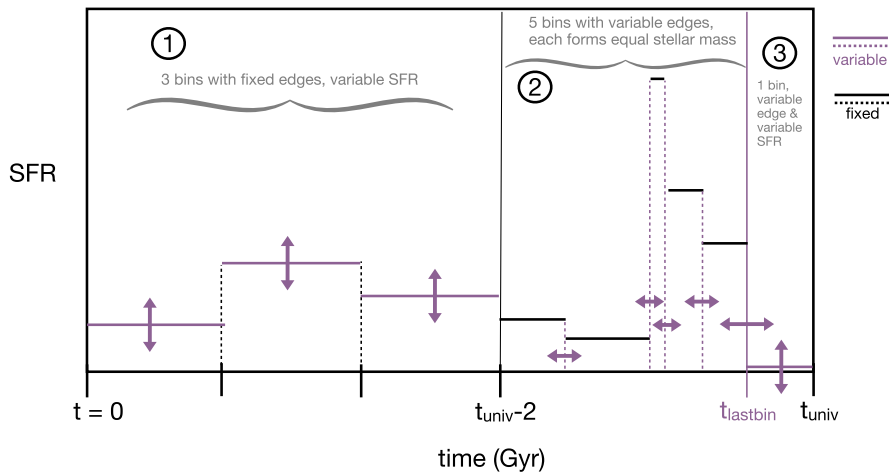


Figure 7. Graphical representation of the SFH model used in this work. The model consists of three parts: the oldest section contains three bins with variable SFR but fixed edges, the middle section contains five bins with variable edges, and the most recent portion is modeled as a single bin with free width and SFR. Purple lines with arrows are used to indicate quantities that are allowed to vary; black lines indicate fixed quantities.

However, we do not include the WISE 12 and 24 μm photometry in our fit. Alatalo et al. (2017) shows that post-starburst galaxies in the local universe have complex and unusual mid-infrared properties: the WISE photometry of these galaxies cannot be reproduced by starlight alone, but appears to be significantly influenced by emission from active galactic nuclei (AGN), polycyclic aromatic hydrocarbon (PAH) features, and/or asymptotic giant branch (AGB) dust. Due to the complex and still poorly understood nature of this part of the spectrum, in particular for post-starburst galaxies, the mid-IR data points will not help constrain the properties we aim to address in this paper. We ensured that excluding these points did not bias our recovered SFRs: for a randomly selected subsample of ~ 100 galaxies, there was no significant difference in the median SFR in fits where we included or excluded the WISE 12 μm and 24 μm photometry. Further analysis of the mid-IR data points are beyond the scope of this paper and will be subject to a future investigation. We discuss the WISE properties of our sample further in Section 3.3.

In addition to seven-band photometry, we fit the SDSS spectrum of each galaxy. We aperture-correct the spectrum using the observed SDSS photometry in the *gri* bands. We note that at $z \sim 0.7$, the diameter of the SDSS/BOSS fiber is larger than the effective radius of these compact post-starburst galaxies, and thus the SDSS spectrum includes the majority of the light from each galaxy; our median aperture correction is a factor of 1.3. Maltby et al. (2018), Suess et al. (2020), and Setton et al. (2020) find that post-starburst galaxies have flat color gradients across similar spatial scales as the SDSS fiber, indicating that the aperture-corrected SDSS spectra are likely accurate reflections of the total integrated stellar light from these galaxies.

In our fits, we mask all spectral pixels within 50 \AA of the 3727 \AA [O II] line, or within 100 \AA of the 5007 \AA [O III] line. Previous studies have found that [O II] emission in post-starburst galaxies is primarily caused by LINER or AGN activity (e.g., Yan et al. 2006; Lemaux et al. 2010). Greene et al. (2020) showed that some SQuIGGLE galaxies have extreme [O III] equivalent widths, again due to the presence of AGN. Because it is currently not possible to model the AGN contribution to these forbidden lines in *Prospector*, we mask them in our fits. Unobscured AGN are too blue to fall into

our color-based selection algorithm (Section 2). While Greene et al. (2020) does find an elevated occurrence rate of obscured AGN in our sample, the continuum emission of all but the very most luminous obscured AGN is dominated by galaxy light. Masking [O II] and [O III] thus ensures that our fitting results are not dominated by AGN emission.

3.2. SED Fitting Results

Here, we show the results of our SED fitting to the full SQuIGGLE sample. Best-fit SED fitting parameters for all galaxies are listed in Table 2. Figure 8 shows example *Prospector* fits to three galaxies in SQuIGGLE. The upper-left panel shows the observed and best-fit SDSS and WISE photometry. The upper-right panel shows the observed SDSS spectrum and the best-fit stellar population model. The lower-left panel shows the derived SFH. As an alternate way of viewing the SFH, the lower-right panel shows the cumulative mass fraction formed as a function of time. The shaded vertical blue region in the third and fourth columns marks the recent starburst (using the derivative-based method described in detail in Suess et al. 2021, in preparation). This figure illustrates that our data and modeling framework are able to place strong constraints on the SFH for each galaxy.

Figure 9 shows histograms of derived properties for the full SQuIGGLE sample. These fits confirm that SQuIGGLE galaxies are massive; nearly all galaxies in the sample have $M_* \gtrsim 10^{11} M_\odot$. This is not unexpected: these $z > 0.5$ galaxies had to be bright enough to be targeted spectroscopically by SDSS and meet our $S/N \geq 6$ criterion. While lower-mass post-starburst galaxies may exist at $z \sim 0.7$, they would not be included in our sample; SQuIGGLE was designed to select bright, massive, and burst-dominated galaxies that can serve as testbeds for the fast quenching process. SQuIGGLE galaxies are likely the most extreme examples of what may be a much larger population of quenching galaxies. We also see that—as expected—the majority of SQuIGGLE galaxies are relatively dust-free, with a median $A_V \sim 0.3$ mag. Very dusty post-starburst galaxies are generally too red to fall into our color-based sample selection (Section 2; Figure 6). The best-fit metallicities tend to be slightly supersolar, as expected for massive galaxies according to the Gallazzi et al. (2005) mass–

Table 2
Prospector Spectral Energy Distribution (SED) Fitting Results for SQuIGGLE Post-starburst Galaxies

SDSS ID	$\log M_*/M_\odot$	$\log Z/Z_\odot$	A_v (mag) ^a	dust index ^a	t_q (Myr)	f_{burst}
spec-6137-56270-0195	11.40 ^{+0.07} _{-0.11}	0.55 ^{+0.09} _{-0.10}	0.86 ^{+0.15} _{-0.09}	0.20 ^{+0.07} _{-0.10}	106 ⁺¹⁷ ₋₂₆	0.36 ^{+0.24} _{-0.10}
spec-0978-52431-0077	11.31 ^{+0.06} _{-0.03}	0.20 ^{+0.32} _{-0.07}	0.44 ^{+0.07} _{-0.05}	-0.00 ^{+0.19} _{-0.14}	165 ⁺⁹ ₋₅₂	0.42 ^{+0.07} _{-0.13}
spec-5192-56066-0419	11.44 ^{+0.06} _{-0.06}	-0.02 ^{+0.10} _{-0.11}	0.34 ^{+0.07} _{-0.06}	-0.69 ^{+0.23} _{-0.18}	495 ⁺¹²³ ₋₁₂₆	0.51 ^{+0.28} _{-0.16}
spec-5288-55865-0858	11.05 ^{+0.07} _{-0.08}	0.28 ^{+0.10} _{-0.07}	0.58 ^{+0.10} _{-0.10}	-0.21 ^{+0.17} _{-0.15}	183 ⁺²¹ ₋₂₄	0.38 ^{+0.12} _{-0.13}
spec-4575-55590-0605	11.30 ^{+0.04} _{-0.05}	0.06 ^{+0.06} _{-0.06}	0.37 ^{+0.07} _{-0.07}	-0.03 ^{+0.18} _{-0.17}	480 ⁺⁸⁸ ₋₁₁₅	0.41 ^{+0.15} _{-0.08}
spec-3817-55277-0279	11.59 ^{+0.03} _{-0.03}	-0.28 ^{+0.09} _{-0.08}	0.17 ^{+0.03} _{-0.03}	-0.71 ^{+0.23} _{-0.18}	715 ⁺⁵²¹ ₋₂₁₇	0.98 ^{+0.02} _{-0.23}
spec-5140-55836-0177	11.23 ^{+0.04} _{-0.03}	0.24 ^{+0.18} _{-0.11}	0.23 ^{+0.05} _{-0.06}	-0.45 ^{+0.30} _{-0.27}	217 ⁺¹⁰² ₋₈₁	0.70 ^{+0.13} _{-0.19}
spec-1630-54476-0502	11.56 ^{+0.04} _{-0.08}	0.12 ^{+0.09} _{-0.07}	0.35 ^{+0.06} _{-0.07}	0.22 ^{+0.12} _{-0.19}	55 ⁺¹⁴ ₋₁₃	0.15 ^{+0.23} _{-0.03}
spec-3754-55488-0041	11.54 ^{+0.03} _{-0.05}	0.21 ^{+0.10} _{-0.11}	0.15 ^{+0.07} _{-0.06}	-0.48 ^{+0.42} _{-0.36}	358 ⁺¹⁰⁵ ₋₉₀	0.16 ^{+0.13} _{-0.04}
spec-6649-56364-0311	11.47 ^{+0.04} _{-0.09}	-0.01 ^{+0.18} _{-0.17}	0.17 ^{+0.05} _{-0.07}	-0.44 ^{+0.31} _{-0.29}	352 ⁺¹¹⁵ ₋₁₁₅	0.23 ^{+0.34} _{-0.09}
spec-5048-56218-0165	11.53 ^{+0.04} _{-0.05}	0.03 ^{+0.08} _{-0.09}	0.52 ^{+0.09} _{-0.07}	-0.44 ^{+0.24} _{-0.23}	271 ⁺¹³⁹ ₋₉₄	0.32 ^{+0.17} _{-0.10}
spec-6054-56089-0547	11.65 ^{+0.02} _{-0.03}	0.71 ^{+0.09} _{-0.10}	0.14 ^{+0.04} _{-0.04}	-0.18 ^{+0.25} _{-0.21}	94 ⁺³⁴ ₋₂₂	0.19 ^{+0.03} _{-0.03}
spec-4403-55536-0765	11.50 ^{+0.05} _{-0.04}	0.15 ^{+0.13} _{-0.08}	1.24 ^{+0.07} _{-0.08}	0.11 ^{+0.09} _{-0.09}	38 ⁺²⁰ ₋₁₄	0.56 ^{+0.13} _{-0.11}
spec-6032-56067-0159	11.16 ^{+0.04} _{-0.05}	0.37 ^{+0.19} _{-0.21}	0.28 ^{+0.08} _{-0.08}	-0.33 ^{+0.22} _{-0.34}	147 ⁺⁵² ₋₅₁	0.32 ^{+0.11} _{-0.08}
spec-6639-56385-0597	11.54 ^{+0.02} _{-0.03}	0.00 ^{+0.12} _{-0.08}	0.14 ^{+0.05} _{-0.04}	-0.75 ^{+0.45} _{-0.18}	159 ⁺⁴⁴ ₋₃₂	0.47 ^{+0.20} _{-0.08}
spec-4013-55629-0073	11.48 ^{+0.05} _{-0.06}	0.15 ^{+0.16} _{-0.11}	0.08 ^{+0.06} _{-0.04}	-0.21 ^{+0.32} _{-0.41}	150 ⁺⁷⁷ ₋₄₈	0.32 ^{+0.39} _{-0.09}
spec-5993-56070-0251	11.46 ^{+0.06} _{-0.08}	0.24 ^{+0.15} _{-0.10}	0.30 ^{+0.13} _{-0.10}	-0.40 ^{+0.32} _{-0.29}	130 ⁺⁵⁸ ₋₃₇	0.33 ^{+0.29} _{-0.11}
spec-5014-55717-0745	11.32 ^{+0.07} _{-0.07}	0.04 ^{+0.14} _{-0.13}	0.54 ^{+0.12} _{-0.12}	0.13 ^{+0.19} _{-0.30}	195 ⁺¹⁷⁹ ₋₇₃	0.43 ^{+0.35} _{-0.21}
spec-5291-55947-0601	11.30 ^{+0.10} _{-0.06}	0.13 ^{+0.08} _{-0.07}	0.26 ^{+0.07} _{-0.09}	-0.38 ^{+0.24} _{-0.31}	47 ⁺³⁴ ₋₁₅	0.44 ^{+0.49} _{-0.34}
spec-5475-56011-0379	11.60 ^{+0.04} _{-0.07}	0.05 ^{+0.05} _{-0.05}	0.37 ^{+0.08} _{-0.06}	-0.34 ^{+0.16} _{-0.15}	76 ⁺³⁶ ₋₂₆	0.33 ^{+0.61} _{-0.14}
...

Note.

^a Assuming the Kriek et al. (2010) dust law.

(This table is available in its entirety in machine-readable form.)

metallicity prior we used in the fits. We see a wide range of dust indices, roughly spanning the prior range allowed in our fits. This is likely because our data have relatively little leverage on this parameter due to our short wavelength range and lack of UV and IR data. These massive galaxies have relatively high velocity dispersions, $\sigma \sim 200 \text{ km s}^{-1}$, as expected from the pPXF results we used as a prior (Greene et al. 2020).

3.2.1. SED SFRs

Next, we use the `Prospector` fitting results to investigate where the SQuIGGLE sample lies in relation to the star-forming main sequence: is star formation truly suppressed in these post-starburst galaxies? SED-based SFRs are notoriously tricky to calculate, and depend sensitively on the assumed SFH (e.g., Lee et al. 2009, 2010; Maraston et al. 2010; Wuyts et al. 2011). It is therefore *essential* that we test our SFH model and fitting framework before relying on SED SFRs. A forthcoming paper, Suess et al. (2021, in preparation), fits the mock galaxies described in Section 2.2 and investigates how well the output SFHs capture the ongoing SFRs of the mock post-starburst galaxies. We find that SFRs above $1 M_\odot \text{ yr}^{-1}$ are slightly underestimated ($\lesssim 0.1$ dex median offset) but generally recovered well, with ~ 0.15 dex of scatter. However, below $1 M_\odot \text{ yr}^{-1}$, the data do not have significant constraining power on the SFR. Given the high stellar masses of our galaxies, this limit corresponds to very low sSFRs of $\lesssim 10^{-11} \text{ yr}^{-1}$. Higher-quality spectra and/or additional wavelength coverage would likely be required to recover lower levels of ongoing star formation.

Figure 10 shows the derived SFRs as a function of stellar mass for all galaxies in the SQuIGGLE sample. The shaded

blue bar indicates the star-forming main sequence from Whitaker et al. (2012b). The dashed black line shows the reliability limit of our SFR measurements. The median SFR of the SQuIGGLE galaxies is *below* our detectability threshold: the majority of SQuIGGLE galaxies have $1 M_\odot \text{ yr}^{-1}$ or less of ongoing star formation. This is more than an order-of-magnitude offset from the star-forming main sequence, which lies at $\sim 40 M_\odot \text{ yr}^{-1}$ at this mass and redshift. While several galaxies in our sample do have higher ongoing SFRs, these galaxies are rare: just $\sim 2\%$ of SQuIGGLE galaxies have SFRs on or above the star-forming main sequence.

We note that these SFRs are based on photometry with $\lambda_{\text{rest}} \lesssim 12 \mu\text{m}$, and thus we cannot exclude the possibility that these objects host some amount of additional star formation that is fully obscured by dust. This would require optically thick dust: otherwise, dusty star-forming galaxies have $B_m - V_m$ colors that are too red to fall into our selection algorithm. Observations at rest-frame infrared or longer wavelengths, such as those described in Section 6, are required to fully rule out higher obscured SFRs (additionally see, e.g., Alatalo et al. 2017 and Smercina et al. 2018 for a discussion of the mid- and far-infrared properties of K+A galaxies). While in Section 3.3 we show that most of our sample is undetected in W4, these upper limits do not allow us to eliminate the possibility that some SQuIGGLE galaxies could be highly dust-obscured star-formers.

3.2.2. Properties of the Recent Burst

The flexibility of our SFH model allows us to characterize the recent starburst. As described in detail in Section 3.1, we define the burst start and end based on the time derivative of the output SFH. Our modeling framework is able to accurately

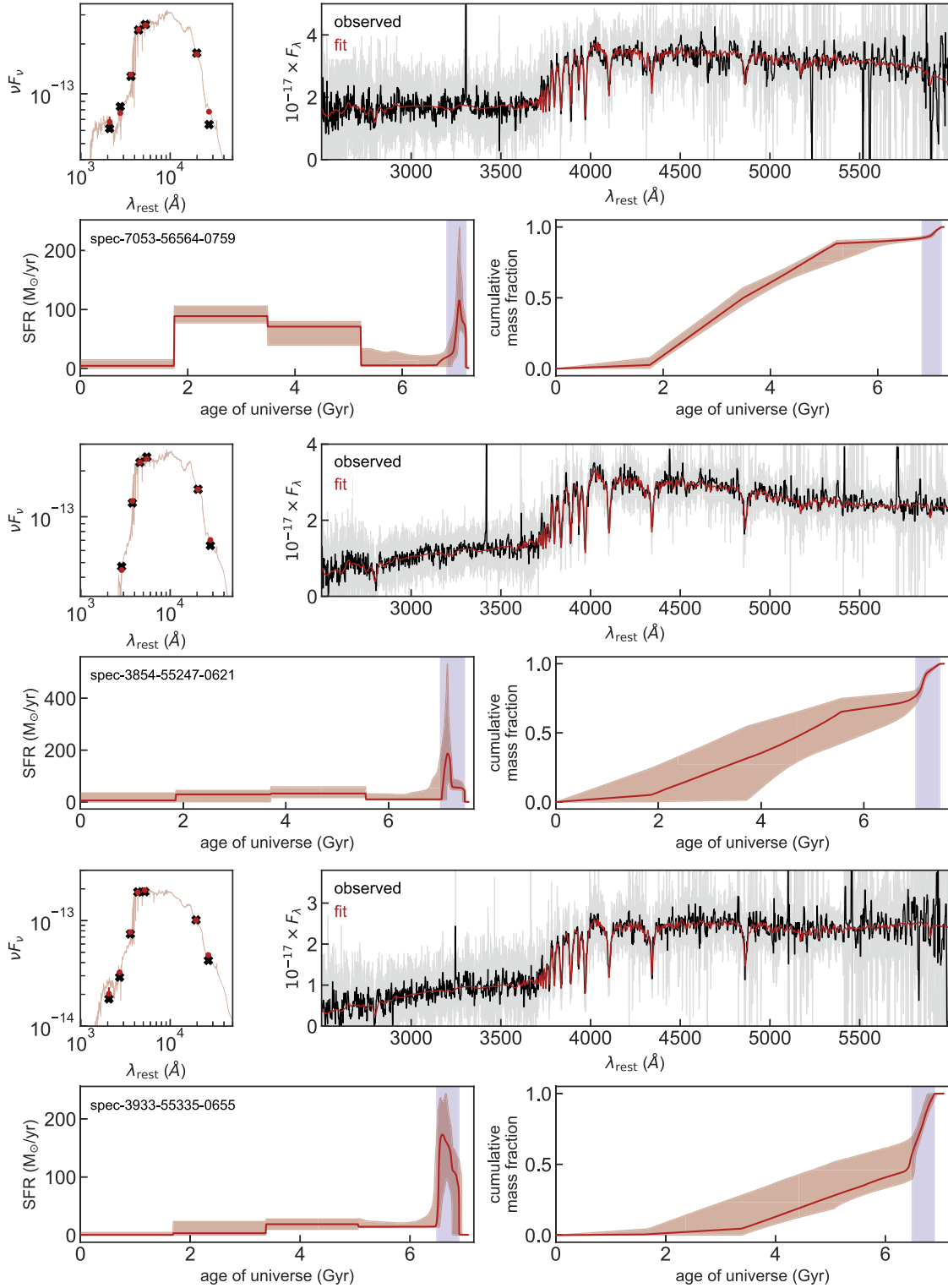


Figure 8. Three example fits using our *Prospector* model, chosen to roughly span the observed range in t_q and f_{burst} . The fits are ordered by increasing t_q . The upper-left panel shows the observed (black cross) and best-fit (red point) SDSS and WISE photometry. The upper-right panel shows the observed spectrum (gray), a 7 pixel median boxcar smoothed version of the observed spectrum (black), and the best-fit spectrum (red). The lower-left panel shows the derived SFH and its 16th–84th percentile confidence interval; the blue shaded region represents the “burst” defined using a derivative-based threshold described in the text. The lower-right panel shows the cumulative fraction of the mass formed over time; again, the burst is shaded in blue.

infer the end time of the recent burst (t_q) with a scatter of just 0.06 dex, as demonstrated in Suess et al. (2021, in preparation). We are also able to place conservative limits on the mass fraction formed in the recent burst: while our recovered mass fractions tend to saturate at $\sim 60\%$, we are able to recover lower

burst mass fractions with high fidelity (scatter ~ 0.1 dex). This saturation is likely due to the fact that our prior assumes that the SFH follows the average UniverseMachine SFH of a massive quiescent galaxy (Behroozi et al. 2019). This effectively asserts that these quenched galaxies likely formed a significant amount

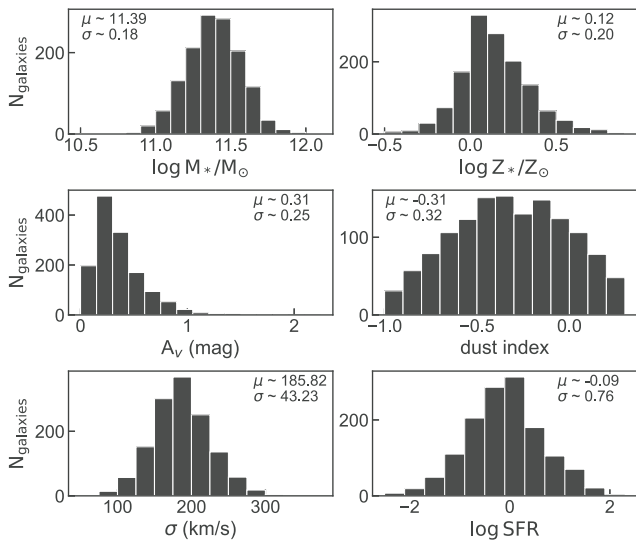


Figure 9. Histograms of recovered properties from SED fitting. The median and standard deviation of each parameter are shown in the upper-left or right corner of the plot. SQuIGGLE galaxies tend to have very high stellar masses and relatively low dust attenuation.

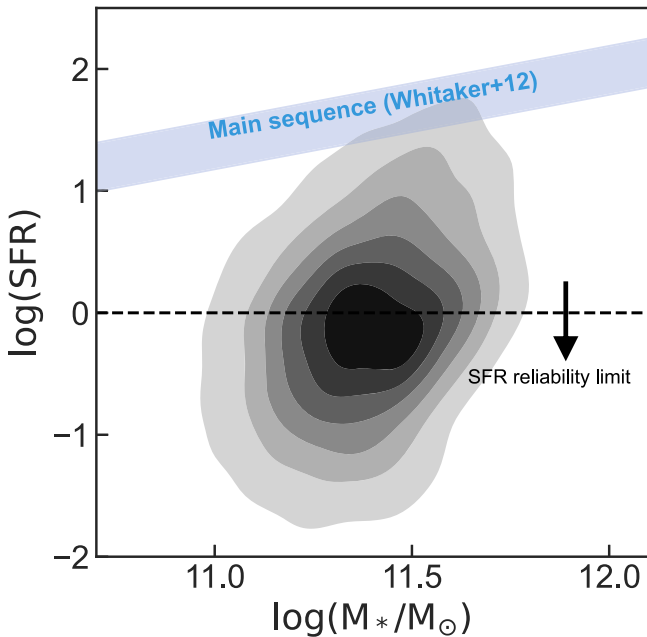


Figure 10. Star formation rate as a function of stellar mass for SQuIGGLE galaxies (contours), compared to the $z = 0.7$ star-forming main sequence from Whitaker et al. (2012b; blue shaded region). The contours are evenly spaced between 10% and 85% of the full distribution of best-fit SFRs. All recovered SFRs below $1 M_{\odot} \text{ yr}^{-1}$ should be treated as upper limits at $1 M_{\odot} \text{ yr}^{-1}$; our spectra and fitting methods cannot distinguish between lower levels of ongoing star formation. Galaxies in SQuIGGLE are quenched, with the majority of galaxies lying more than an order of magnitude below the main sequence. Just 2% of post-starburst galaxies in our color-selected sample have SFRs on or above the main sequence.

of their mass at early times. This choice allows our model to effectively “hide” a large number of old, red stars under a large recent burst, disfavoring extremely high burst mass fractions.

Figure 11 shows the time since quenching (t_q) as a function of the burst mass fraction (f_{burst}). These SED fitting results allow us to confirm that SQuIGGLE galaxies recently quenched a major epoch of star formation. The quenching

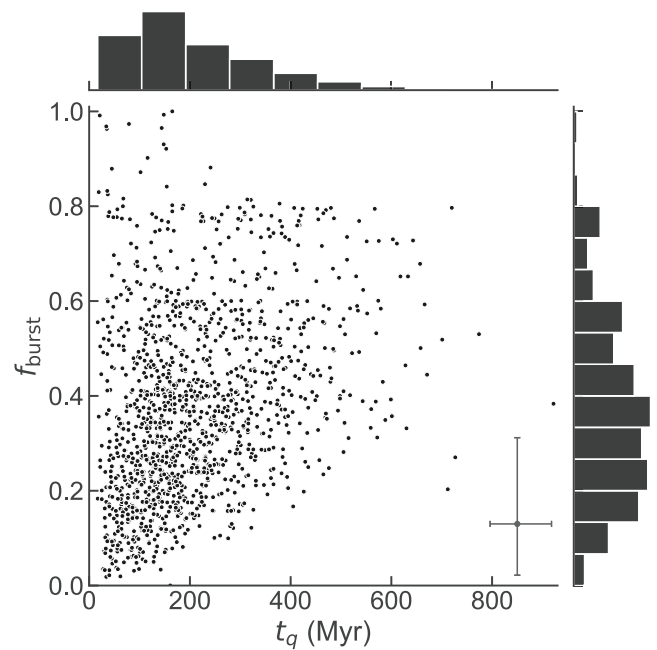


Figure 11. Burst mass fraction vs. time since quenching for all SQuIGGLE galaxies; histograms show the marginal distribution of each parameter. The point in the lower right shows a typical error bar; we note that the error on f_{burst} is typically asymmetric, with a higher tail toward high burst mass fractions. SQuIGGLE galaxies have a wide range of burst mass fractions and quenching timescales. However, galaxies that quenched longer ago are only included in our sample if they also have high burst mass fractions; galaxies with high t_q and low f_{burst} are likely too red to satisfy our color-based selection criteria.

timescale distribution peaks at ~ 175 Myr, with a tail toward longer quenching times. Galaxies that quenched >400 Myr ago make up just 9% of the SQuIGGLE sample. As expected based on their spectral shapes (Figure 3), our post-starburst sample does not include any galaxies that quenched more than a gigayear before observation. We find that galaxies with large t_q values are included in our sample only if they also have relatively high f_{burst} values (as expected from Figure 6). The 16th–84th percentile range on our inferred t_q values is ~ 80 – 350 Myr, which corresponds to the main-sequence lifetimes of ~ 4 – $7 M_{\odot}$ stars. Thus, $\sim 7 M_{\odot}$ stars are generally the most massive stars we expect to be alive in SQuIGGLE galaxies. This stellar mass corresponds roughly to the B4V classification, which is the boundary where stellar spectra begin to show very deep Balmer lines and strong Balmer breaks—exactly the spectral shapes we selected for. Our shortest recovered t_q values are thus consistent with the main-sequence lifetimes of the highest-mass stars we would expect to find in these galaxies.

Figure 11 also illustrates that, while SQuIGGLE galaxies have a large range in burst mass fractions, in general these galaxies recently concluded a major burst. More than 75% of SQuIGGLE galaxies formed at least a quarter of their total stellar mass during the recent burst, and 20% of SQuIGGLE galaxies formed *more than half* of their total stellar mass in the recent burst. Despite our relatively conservative priors on burst mass fraction, we find that SQuIGGLE galaxies appear to be much more burst-dominated than local post-starburst galaxies; French et al. (2018) found that $z \sim 0$ post-starburst galaxies often formed just $\sim 10\%$ – 15% of their mass during the recent starburst. By going to intermediate redshift, we were able to identify the tail end of the peak quenching era at cosmic noon.

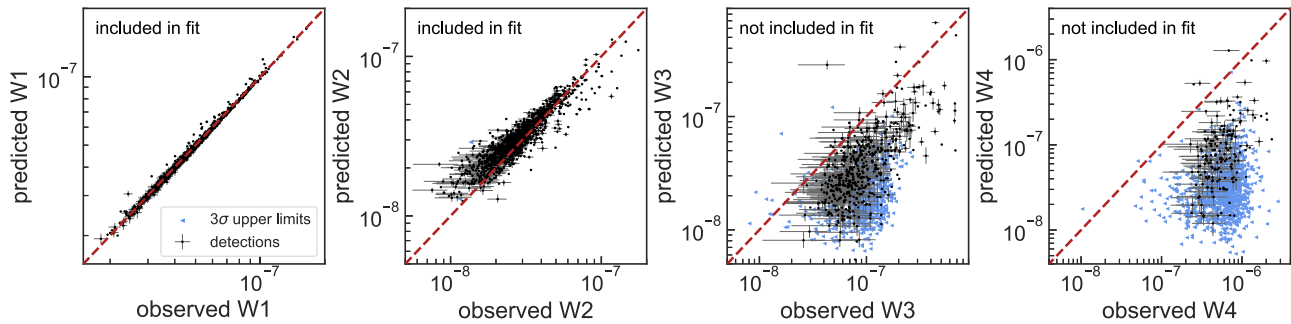


Figure 12. Predicted vs. observed WISE fluxes. Non-detections are indicated with blue triangles. While both W1 ($3.4 \mu\text{m}$) and W2 ($4.6 \mu\text{m}$) are well-predicted by our `Prospector` modeling, we find that SQuIGGLE galaxies detected in the W3 ($12 \mu\text{m}$) and W4 ($22 \mu\text{m}$) bands tend to have much higher fluxes than predicted.

3.3. SQuIGGLE Galaxies Have Anomalous Mid-infrared Properties

In the local universe, several studies have found that post-starburst galaxies have unusual mid-infrared properties. Alatalo et al. (2017) showed that $z < 0.3$ post-starburst galaxies have strong infrared emission, shallow [3.4]–[4.6] colors, and flat or rising slopes at [12]–[22]. These properties are unlikely to be produced through star formation alone, and indicate the presence of AGN, strong PAH features, and/or significant contributions from dust-enshrouded AGB stars. Smercina et al. (2018) showed that $z \sim 0$ post-starburst galaxies exhibit high PAH abundances and very strong PAH features as well as large reservoirs of warm dust indicating atypical radiation fields. These features are unusual for either star-forming or quiescent galaxies, and indicate that a “standard” SED fitting setup is unlikely to accurately reproduce the mid-infrared properties of post-starburst galaxies.

These results lead us to question whether the post-starburst galaxies in SQuIGGLE may have unusually high WISE fluxes or anomalous WISE colors. Because the exact nature of the processes contributing to this mid-IR flux is uncertain, we did *not* include the WISE $12 \mu\text{m}$ (W3) or $22 \mu\text{m}$ (W4) photometry in our SED fitting. Here, we test whether the predicted WISE photometry from our `Prospector` modeling matches the observed data points.

We first carefully flag which SQuIGGLE galaxies are detected in the W3 and W4 bands. We consider all W3 and W4 measurements $\geq 3\sigma$ to be detections. Because W1 and W2 are both significantly more sensitive than W3/W4 and have much better characterized PSFs, we then use the positions of W1 and W2 sources to confirm lower-S/N W3 and W4 sources. We consider W3 and W4 measurements at $>1.7\sigma$ ($>90\%$ confidence) to be detections if they correspond to a W1/W2 source detected at $>2.5\sigma$. While individually these lower-S/N sources would not be formal detections, the combination of multiple bands of WISE imaging results in a robust $>3\sigma$ identification of a source, albeit with large uncertainties on the individual WISE fluxes. For all sources that do not meet these criteria, we set robust 3σ upper limits on the W3 and W4 flux based on the measured background in the WISE bands. In total, we find that 511 SQuIGGLE galaxies are detected in W3 and 176 are detected in W4.

Figure 12 shows the WISE fluxes predicted from our `Prospector` modeling as a function of the observed WISE fluxes. The left two panels show W1 ($3.4 \mu\text{m}$) and W2 ($4.6 \mu\text{m}$), both of which are included in our `Prospector` fits; the right two panels show W3 ($12 \mu\text{m}$) and W4 ($22 \mu\text{m}$), which are *not* included in our fitting. The dashed red line in each panel

shows the one-to-one relation. We find that the observed W1 and W2 values are well-matched by our fits, with a <0.005 dex offset in W1 and a 0.03 dex offset in W2. However, the fluxes of SQuIGGLE galaxies that are detected in W3 and W4 tend to be significantly underpredicted by our modeling. In W3, detected galaxies have fluxes ~ 0.4 dex higher than our predictions; for W4 detections, the observations are ~ 0.8 dex higher than the predictions. We note that including the W3 and W4 data points in our modeling does not resolve these offsets, indicating that the mid-infrared properties of these galaxies cannot be captured by our modeling framework. Understanding the nature of this excess mid-infrared flux is beyond the scope of this work, and will be studied in future SQuIGGLE papers.

4. SFRs from Lines

In this section, we compare the SFRs obtained by our SED fitting (Figure 10) with several alternate techniques for estimating SFRs based on optical lines; our goal here is to compare our `Prospector` SFRs with other SFR indicators commonly used in the literature. Two spectral features in the SDSS wavelength regime— $H\beta$ and $[\text{O II}]\lambda 3727$ —are often used as SFR indicators. Both of these lines are imperfect SFR indicators for post-starburst galaxies. First, due to the strong A-star signatures of our post-starburst galaxies (Figure 3), we typically see $H\beta$ in absorption, not emission. While jointly modeling the continuum absorption along with the line emission can provide estimates of how much $H\beta$ emission is filling in the absorption line, these line flux measurements are extremely difficult for massive galaxies with broad lines. Second, LINER emission can contribute to both $[\text{O II}]$ and $H\beta$ line flux; previous studies have found that this LINER emission is common in post-starburst galaxies (e.g., Lemaux et al. 2010; Kocevski et al. 2011; French et al. 2015). Shocks could also contribute to the ionized emission from galaxies, including $[\text{O II}]$ (e.g., Alatalo et al. 2016; Maddox 2018). In this case, $[\text{O II}]$ and $H\beta$ SFRs should be treated as *upper* limits, as in French et al. (2015): star formation is not the only contributor to the measured line flux. However, both $H\beta$ and $[\text{O II}]$ are affected by dust. The SDSS spectra do not cover the $H\alpha$ regime, and thus our best estimate of the dust attenuation in these galaxies comes from our SED fitting. If these dust values are underestimated, the SFR values should be considered *lower* limits. The competing effects of dust and LINER emission thus make it unclear whether $H\beta$ and $[\text{O II}]$ SFRs should be treated as upper or lower limits for post-starburst galaxies: the answer likely depends on the individual galaxy. For this reason—like Belli et al. (2021)—we conclude that the SED SFRs are more reliable than line-based SFRs for post-starburst galaxies.

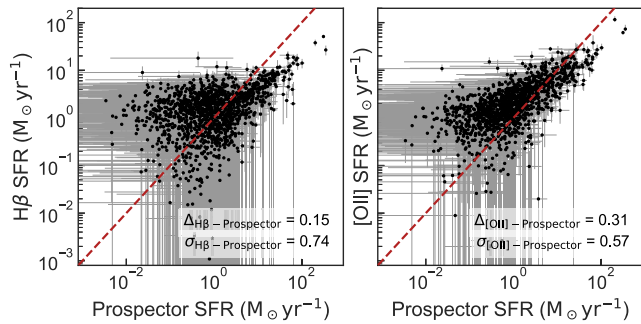


Figure 13. Comparison of SFR measured directly from both the $H\beta$ and $[O II]$ lines with the *Prospector* SFRs described in Section 3. There is significant scatter in both line measurements at the low-SFR end. Toward high SFRs, the $[O II]$ SFRs are offset slightly higher than the *Prospector* SFRs, likely due to LINER contributions; the $H\beta$ SFRs are offset lower than the *Prospector* SFRs.

Nonetheless, here we compute both $H\beta$ and $[O II]$ SFRs to serve as a comparison point for the *Prospector* SFRs calculated in Section 3.

We adopt $H\beta$ line flux measurements from Greene et al. (2020), who used the public Penalized Pixel-Fitting code pPXF (Cappellari & Emsellem 2004) to fit the stellar continuum as well as $H\beta$ and $[O III]$ emission lines. We assume an intrinsic line ratio of $H\alpha/H\beta = 2.86$ to estimate the $H\alpha$ flux. We correct these fluxes for dust using the *Prospector* dust index and A_V values. Again, our fitting assumes that lines (including $H\alpha$ and $H\beta$) are twice as attenuated as the stellar continuum. We then use the Kennicutt (1998b) conversion, adjusted to a Chabrier (2003) IMF, to estimate the SFR. We note that our *Prospector* fits include the $H\beta$ line, and thus this line is also a major contributor to the SFRs shown in Figure 10. However, the Kennicutt (1998b) conversion assumes solar metallicity and a constant SFH, whereas the *Prospector* SFRs takes into account the metallicity and SFH.

To calculate $[O II]$ SFRs, we measure the aperture-corrected flux from the $[O II]$ doublet by modeling the region of the spectrum around the line with a single Gaussian centered at the mean wavelength of the $[O II]$ doublet plus a straight-line fit to the continuum. Our spectra do not resolve the $[O II]$ doublet. We hold the width of the Gaussian line profile fixed to the velocity as measured by pPXF (Greene et al. 2020). Again, we correct the measured line flux for dust extinction using the *Prospector* fitting results. Finally, we used the conversion in Kennicutt (1998b; adjusted to a Chabrier 2003 IMF) to convert our measured line flux to an SFR. Error bars on the SFR were obtained using 1000 bootstrap realizations of the measured line flux.

Figure 13 shows the SFR estimated from both $H\beta$ (left) and $[O II]$ (right) as a function of the *Prospector* SFR (Section 3). Again, our mock recovery tests indicate that *Prospector* SFRs do not have significant constraining power below $1 M_\odot \text{ yr}^{-1}$. We see that, while the line-based SFRs generally correlate with the *Prospector* SFRs, there is a large amount of scatter, particularly at the low-SFR end. $H\beta$ SFRs are typically higher than *Prospector* SFRs at low SFRs, likely because the $H\beta$ fluxes in this regime are dominated by spectral noise. At high SFR, $H\beta$ SFRs are offset lower than the *Prospector* SFRs; this could be due to the fact that the *Prospector* SFRs do not assume a constant SFH and solar metallicity, as the Kennicutt (1998b) conversion does. Median $[O II]$ SFRs are offset slightly from

Prospector SFRs at all SFRs. This difference is largest at the lowest SFRs, likely due to an increasing fraction of $[O II]$ flux originating from LINER emission. For all three SFR indicators, only a small fraction ($\sim 2\%$) of SQuIGGLE galaxies have high SFRs consistent with the star-forming main sequence. Because of the effects of both LINER emission and dust, we take the *Prospector* SFRs as the most reliable SFR indicator available for the full SQuIGGLE sample (see also, e.g., Belli et al. 2021). However, we note that no matter which SFR indicator is used—*Prospector*, $H\beta$, or $[O II]$ —the median SFR of all galaxies in the SQuIGGLE sample is an order of magnitude or more below the main sequence.

5. Comparison to Other Samples of PSBs

Here, we place the SQuIGGLE sample in the context of existing large samples of post-starburst galaxies. As discussed in Section 2, myriad studies have selected recently quenched galaxies across redshift by their spectral line strengths, spectral shapes, or colors. The largest spectroscopic samples of post-starburst galaxies come from the low-redshift universe, $z \lesssim 0.2$, where large spectroscopic surveys such as the SDSS allow for the identification of rare recently quenched galaxies (e.g., Zabludoff et al. 1996; Quintero et al. 2004; French et al. 2015; Alatalo et al. 2016). While post-starburst galaxies are common at $z \gtrsim 1$ (e.g., Whitaker et al. 2012a; Wild et al. 2016; Belli et al. 2019), spectroscopic samples tend to be smaller due to the difficulty of high-redshift spectroscopy. The only other large intermediate-redshift spectroscopic sample of post-starburst galaxies comes from Pattarakijwanich et al. (2016), who also select from the SDSS and BOSS surveys. In Section 5.1, we compare SQuIGGLE to lower- and higher-redshift samples; in Section 5.2, we compare SQuIGGLE to the Pattarakijwanich et al. (2016) sample at the same redshift.

5.1. Comparison to Post-starburst Samples across Redshift

Figure 14 shows the SQuIGGLE sample in context of one low-redshift (French et al. 2015) and one high-redshift (Wild et al. 2020) sample of post-starburst galaxies. The French et al. (2015) sample was selected by their high $H\delta$ and low $H\alpha$ equivalent widths, while the Wild et al. (2020) sample was selected using a PCA technique. Figure 14 shows that SQuIGGLE galaxies lie at intermediate redshift, and tend to have higher stellar masses than many of the French et al. (2015) or Wild et al. (2020) galaxies. The lack of low-mass galaxies in SQuIGGLE compared to lower-redshift studies is likely a selection effect (e.g., Malmquist bias): the galaxies our sample *must* have had high mass in order to fall into the SDSS spectroscopic sample and exceed our S/N cut. While the three populations of post-starburst galaxies overlap significantly in $H\delta - D_n4000$ space, the bulk of the SQuIGGLE galaxies lie at slightly higher $H\delta_A$ values than the French et al. (2015) or Wild et al. (2020) samples. Because stellar age typically increases toward the lower right of this diagram, this indicates that SQuIGGLE galaxies are slightly *younger* on average than either of these samples. This is confirmed by SFH modeling: both Wild et al. (2020) and French et al. (2018) found older post-burst ages for their samples than we find in Section 3. However, it is difficult to directly compare the inferred t_q values because each study uses a slightly different SFH parameterization and definition of t_q .

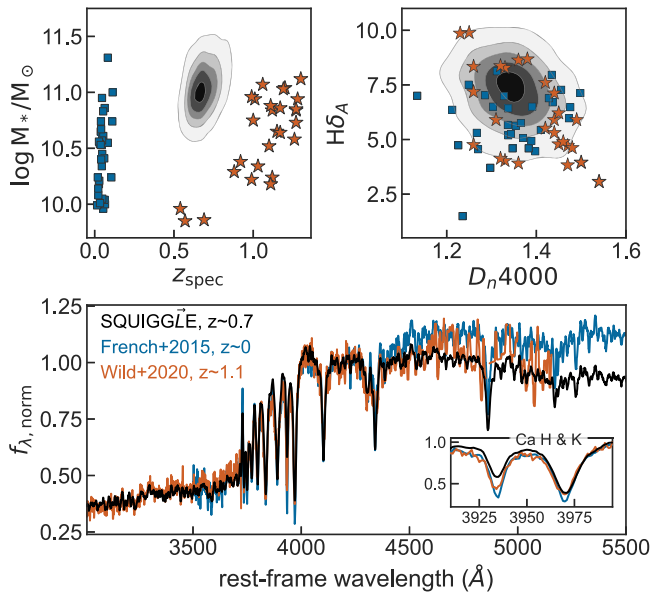


Figure 14. Comparison between the SQuIGGLE sample (black) and other samples of post-starburst galaxies, including the French et al. (2015) sample of $z \sim 0$ galaxies (blue) and the higher-redshift sample from Wild et al. (2020; orange). The SQuIGGLE sample lies at high stellar mass and intermediate redshift. The bulk of SQuIGGLE galaxies have similar D_n4000 values but slightly higher $H\delta$ values than either the Wild et al. (2020) or French et al. (2015) samples, indicating slightly younger stellar ages. The French et al. (2015) and Wild et al. (2020) stacks show slightly more flux at $\lambda_{\text{rest}} > 4500$ Å and more symmetric Ca H and K features than the SQuIGGLE stack; these differences likely reflect a higher fraction of older stars.

The bottom panel of Figure 14 shows a stack of the spectra in all three samples. Both the SQuIGGLE and French et al. (2015) stacks are created using public SDSS data. As in Figure 3, all individual spectra are normalized using the flux between 4150 and 4250 Å. Spectra from the Wild et al. (2020) sample come from both the UDSz ESO Large Programme (PI: Almaini) and Maltby et al. (2016). D. Maltby et al. (2021, in preparation) provides further details about the spectroscopic data reduction. In addition to normalizing the Wild et al. (2020) spectra (again, between 4150 and 4250 Å), we smooth the stack using a 9 pixel median filter past ~ 4300 Å, where fewer than 15 spectra have wavelength coverage. We do not show the Wild et al. (2020) stacked spectrum past ~ 5150 Å, where fewer than five individual spectra have wavelength coverage.

We see two notable differences in the stacked spectra shown in Figure 14: the depth of the absorption lines, and the spectral shape redward of ~ 4400 Å. The calcium H and K lines are deep and nearly symmetric for the French et al. (2015) stack, while they are shallower and much more asymmetric in the SQuIGGLE stack (because the CaH line is more significantly contaminated by H ϵ). These spectral differences indicate that SQuIGGLE galaxies are younger than the French et al. (2015) galaxies. We also find that the French et al. (2015) spectra have nearly a flat slope redward of ~ 4400 Å, while (by construction) the SQuIGGLE stack shows a relatively blue slope. These differences could be caused by differences in the sample selection technique, redshift evolution in the post-starburst population (e.g., Whitaker et al. 2012a; Wild et al. 2016; Rowlands et al. 2018; Belli et al. 2019) or both. The Wild et al. (2020) stack has a slope intermediate between the French et al. (2015) and SQuIGGLE samples. This difference in slope

indicates that both the French et al. (2015) and Wild et al. (2020) samples contain galaxies with larger contributions from old stars. For the French et al. (2015) sample, this aligns with expectations from the SFH fitting in French et al. (2018): these galaxies have best-fit burst mass fractions that are often $\lesssim 20\%$, lower than the SQuIGGLE burst mass fractions shown in Figure 11. However, Wild et al. (2020) finds burst mass fractions that are often $\sim 60\%–80\%$, above the median burst mass fractions for the SQuIGGLE sample. This difference is likely primarily caused by differences in the fitting methodology and definition of “burst mass fraction” used in Wild et al. (2020) and this paper. Furthermore, the Wild et al. (2020) stack shown in Figure 14 is dominated by low-redshift, lower f_{burst} galaxies at these longer wavelengths.

5.2. Comparison to the Pattarakijwanich et al. (2016) Sample

In Figure 15, we compare the SQuIGGLE sample to the Pattarakijwanich et al. (2016) sample. This study also selected post-starburst galaxies from SDSS spectroscopy. Unlike SQuIGGLE, Pattarakijwanich et al. (2016) used a template-fitting approach to find post-starburst galaxies: galaxies were fit with a sum of both an old (“K”) component and a young (“A”) component, then identified as post-starburst if the light-weighted $A/(A+K)$ ratio exceeded 0.25. Pattarakijwanich et al. (2016) selected spectra from both the SDSS and BOSS surveys, including galaxies with redshifts as low as $z = 0.05$. In Figure 15, to facilitate a direct comparison with SQuIGGLE, we show only galaxies with $z \geq 0.5$. The median stacked spectrum of the $z > 0.5$ Pattarakijwanich et al. (2016) sample has significantly more flux at longer wavelengths; again, this indicates older stellar ages. However, the 16%–84% confidence interval of the Pattarakijwanich et al. (2016) encompasses a large range of spectral slopes. The lower 16% interval encompasses the SQuIGGLE stack, indicating that the Pattarakijwanich et al. (2016) sample includes some post-starburst galaxies as young as those in SQuIGGLE. This larger median age and wider age spread is also reflected in the $H\delta–D_n4000$ values: the median value of the Pattarakijwanich et al. (2016) sample is offset from the SQuIGGLE median, but the distribution is broad and overlaps significantly with SQuIGGLE.

We find that 210 post-starburst galaxies are selected both by SQuIGGLE and Pattarakijwanich et al. (2016). These galaxies reflect the full distribution of SQuIGGLE galaxies: they trace the SQuIGGLE contours in $H\delta–D_n4000$ space, and their stacked spectrum is indistinguishable from the full SQuIGGLE sample. This relatively small number of overlapping galaxies is primarily due to the fact that Pattarakijwanich et al. (2016) selected galaxies from SDSS DR9, whereas the SQuIGGLE selection is performed on SDSS DR14. Nearly half of SQuIGGLE-identified post-starburst galaxies were observed after DR9, and thus could not have been included in Pattarakijwanich et al. (2016).

The right panel of Figure 15 shows the $A/(A+K)$ ratio as calculated by Pattarakijwanich et al. (2016), both for the full Pattarakijwanich et al. (2016) sample and the galaxies selected by both Pattarakijwanich et al. (2016) and SQuIGGLE. SQuIGGLE galaxies have a higher median $A/(A+K)$ ratio than the full Pattarakijwanich et al. (2016) sample, indicating that we are generally selecting more burst-dominated galaxies.

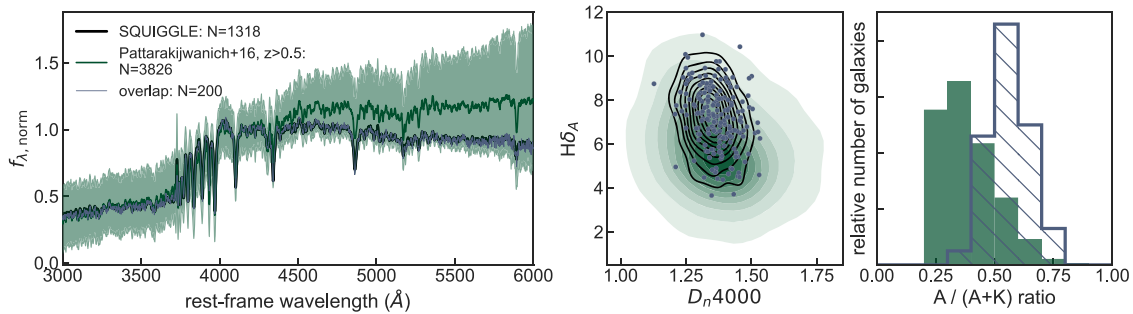


Figure 15. Comparison between the SQuIGGLE sample (black) and the Pattarakijwanich et al. (2016) sample, which is also selected from the SDSS. The left panel shows a stacked spectrum of all SQuIGGLE galaxies (black), all Pattarakijwanich et al. (2016) galaxies with $z \geq 0.5$ (green; 16%–84% range shaded), as well as galaxies identified as post-starburst in *both* samples (blue; overlaps with black spectrum). The central panel shows the same three sets of post-starburst galaxies in $H\delta$ and D_n4000 , with the overlapping sample shown as blue dots. While on average the Pattarakijwanich et al. (2016) sample includes older galaxies with lower burst mass fractions, the distribution of this sample is very broad and the 1σ range just encompasses young post-starburst galaxies like those found by SQuIGGLE. The right panel shows histograms of the $A/(A+K)$ ratio (e.g., the light-weighted fractional contribution of A-type stars) for the full Pattarakijwanich et al. (2016) as well as the overlap between the Pattarakijwanich et al. (2016) and SQuIGGLE samples. The galaxies selected by SQuIGGLE tend to have higher $A/(A+K)$ ratios than the full Pattarakijwanich et al. (2016) sample.

In summary, the SQuIGGLE sample is smaller and more targeted than the Pattarakijwanich et al. (2016) sample: SQuIGGLE consists of uniformly young post-starburst galaxies with a narrow spread in $H\delta$ - D_n4000 space. The Pattarakijwanich et al. (2016) sample includes a wider range of stellar ages, but does not include the majority of young SQuIGGLE galaxies that were observed after DR9.

6. SQuIGGLE Science Objectives

The large sample of bright, intermediate-redshift, recently quenched galaxies in SQuIGGLE enables a wide range of studies into the rapid quenching process. Most of these science cases rely on the stellar population synthesis modeling presented in this paper in combination with other multiwavelength data sets. SQuIGGLE is not intended to be a complete sample of post-starburst galaxies at these redshifts: the selection function is complex, and not conducive to number density studies. Instead, SQuIGGLE was designed to select the brightest, most massive, most burst-dominated post-starburst galaxies at intermediate redshifts. These galaxies serve as *laboratories* to conduct detailed multiwavelength dives into the processes responsible for shutting down star formation. Here, we briefly summarize the primary science objectives of SQuIGGLE.

6.1. Molecular Gas Reservoirs

Theoretical quenching mechanisms generally rely on processes that remove the available fuel for star formation by depleting, heating, or ejecting cold molecular gas reservoirs. One of the primary science objectives of SQuIGGLE is to directly test this assumption. An initial Atacama Large Millimeter/submillimeter Array (ALMA) study of the CO(2–1) emission of two SQuIGGLE post-starburst galaxies revealed abundant gas reservoirs despite low ongoing SFRs (Suess et al. 2017). This result indicates that—contrary to expectations—quenching does not require the total removal of molecular gas. Massive gas reservoirs have also been found in local K+A galaxies (e.g., French et al. 2015; Rowlands et al. 2015; Alatalo et al. 2016; Smercina et al. 2018) as well as several young quiescent galaxies at $1 \lesssim z \lesssim 1.5$ (Belli et al. 2021; Williams et al. 2021). These results have prompted theoretical studies into why star formation is suppressed in post-starburst galaxies (e.g., Davis et al. 2019; Salim et al. 2020).

We are currently conducting an ALMA survey of the molecular gas content of eleven additional SQuIGGLE post-starburst galaxies (Bezanson et al. 2022). This study will allow us to test whether these abundant gas reservoirs are common after quenching, and whether the gas fraction depends on other galaxy properties such as time since quenching (Section 3).

These molecular gas measurements, in combination with SFRs, will allow us to place these galaxies on the Kennicutt–Schmidt relation and investigate how efficiently they are forming stars (e.g., Kennicutt 1998a). As part of this work, we are in the process of obtaining other robust estimators of the SFR in these galaxies. In particular, we are using the Very Large Array to investigate possible highly obscured SFRs, and using Keck/Near-Infrared Echellette Spectrometer to calculate Balmer decrement-corrected $H\alpha$ SFRs.

6.2. Morphologies and Sizes

Some studies predict that quenching can be triggered by a gas-rich major merger: in this scenario, the merger funnels gas to the galaxy’s center where it is consumed in an intense starburst (e.g., Hopkins et al. 2006; Wellons et al. 2015). Deep, high-resolution imaging of SQuIGGLE galaxies will allow us to quantify the fraction of recently quenched galaxies that show signs of recent mergers (including tidal features and asymmetric morphologies). Sazonova et al. (2021) suggests that these disturbed morphologies are common for post-starburst galaxies at $z \sim 0$. Our team has obtained Hubble Space Telescope (HST) WFC3/F125W imaging for three SQuIGGLE galaxies targeted as part of our ALMA survey (Figure 16). These galaxies are clearly disturbed: J2202-0033 has a large tidal feature to the west, and both J0027+0129 and J0912+1523 have nearby companions that may be physically associated. The image of J0912+1523 also reveals that it has a spheroidal component embedded within a disk.

Some previous studies have found that post-starburst galaxies have extremely compact sizes, and may be smaller than their older quiescent counterparts (e.g., Whitaker et al. 2012a; Yano et al. 2016; Almaini et al. 2017). Suess et al. (2020) suggested that these size differences may be primarily caused by the effects of radial color gradients (see also Maltby et al. 2018; Setton et al. 2020). In either case, differences in the sizes and/or color gradients of post-starburst galaxies and older quiescent galaxies could provide clues both to the formation

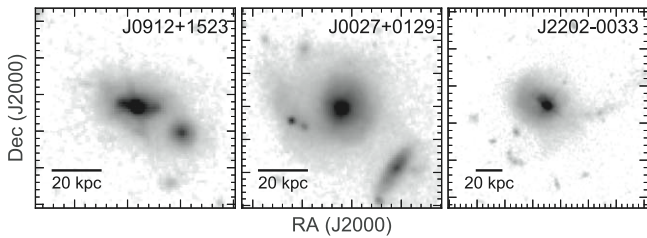


Figure 16. HST/WFC3 F110W images of three galaxies in our sample. We show a 80 kpc square cutout for J0912+1523 and J0027+0129. J2202-0033 is shown in a 150 kpc square cutout to capture the full extent of the tidal tail that stretches to the west. All three galaxies exhibit complex morphologies and merger signatures.

mechanisms for post-starburst galaxies and the processes contributing to evolution along the quiescent sequence. Deep, high-resolution images such as those shown in Figure 16 will allow us to calculate the sizes of SQuIGGLE post-starburst galaxies and compare them to a mass-matched sample of older quiescent galaxies.

While the images presented in Figure 16 shed light on the morphologies and sizes of a few individual SQuIGGLE galaxies, obtaining HST imaging for a statistical sample of post-starburst galaxies is prohibitively expensive. A much larger set of deep, high-resolution images comes from the overlap of the SQuIGGLE sample and the public Hyper SuprimeCam (HSC) survey (Aihara et al. 2018). One of our major science objectives is to use the >150 high-quality HSC images of SQuIGGLE galaxies to investigate the sizes, morphologies, and merger fractions of these recently quenched galaxies (D. Setton et al. in preparation).

6.3. Kinematics

In general, star-forming galaxies tend to be rotationally supported disks, while quiescent galaxies are more likely to be kinematically hot and supported by random motions (e.g., Emsellem et al. 2011). However, it is still not understood why a cessation of star formation correlates with a change in kinematics. Furthermore, it is unclear whether this kinematic transition occurs before, after, or at the same time as star formation shuts down. The bright, recently quenched SQuIGGLE galaxies provide an ideal testbed for integral field unit studies to directly probe the kinematics of galaxies just after quenching. An early result for one SQuIGGLE target (J0912+1523, also shown in Figure 16) revealed that the galaxy is a rotating disk (Hunt et al. 2018). A larger follow-up study of five additional SQuIGGLE galaxies showed that only \sim half of post-starburst galaxies show clear velocity gradients, while the other half are dominated by random motions (Setton et al. 2020).

6.4. Resolved Stellar Populations

Studying the spatially resolved properties of post-starburst galaxies could provide additional clues to the quenching process. Radial age or sSFR gradients can be used to help determine whether quenching proceeded inside-out or outside-in (e.g., Tacchella et al. 2018; Woo & Ellison 2019); radial metallicity gradients can help distinguish between in situ and ex situ components, important when mergers are suggested as a trigger for quenching (e.g., Greene et al. 2015; Chan et al. 2016; Woo & Ellison 2019). Our preliminary study of six

SQuIGGLE galaxies shows that they have flat age gradients as probed by $H\delta$ (Setton et al. 2020). In the absence of strong radial dust or metallicity gradients, these flat age gradients are consistent with the flat color gradients that Maltby et al. (2018) and Suess et al. (2020) find for post-starburst galaxies. Setton et al. (2020) find that these six post-starburst galaxies have young light-weighted ages at all radii, implying that star formation shut off uniformly throughout the galaxy. In the future, we plan to expand the sample size of SQuIGGLE post-starburst galaxies with spatially resolved stellar population measurements; facilities like JWST would be useful to perform these studies further in the infrared, where it is easier to break the age–dust–metallicity degeneracy.

6.5. AGN Incidence

One popular theoretical mechanism for quenching galaxies invokes strong feedback from AGN (e.g., Di Matteo et al. 2005; Hopkins et al. 2006). This feedback, possibly induced by a major merger (Springel et al. 2005; Hopkins et al. 2006; Wellons et al. 2015), could heat the interstellar medium (ISM) and/or drive molecular gas from the galaxy, removing the fuel for star formation (Alatalo et al. 2015). Establishing a direct causal connection between AGN activity and star formation suppression has unfortunately proven difficult, in part because AGN vary dramatically on much shorter timescales than star formation. A large number of AGN surveys have shown that AGN activity depends on SFR and mass (e.g., Hickox et al. 2014). The SQuIGGLE sample allows us to ask how many recently quenched galaxies show AGN activity, and test whether certain types of post-starburst galaxies are more likely to host AGN. Greene et al. (2020) used SQuIGGLE to show that the incidence of AGN depends strongly on D_n4000 : recently quenched galaxies from SQuIGGLE are 10 times more likely to host an optical AGN than a mass-matched sample of older quiescent galaxies. This hints that AGN activity is indeed correlated with the quenching process in these massive galaxies.

6.6. IR Properties

As shown in Figure 12, SQuIGGLE galaxies have puzzlingly high W4 fluxes. At the redshift of SQuIGGLE, W4 corresponds to rest-frame $\sim 11\text{--}14\ \mu\text{m}$. Previous studies at $z \lesssim 0.3$ have found that the mid-infrared spectra of post-starburst galaxies are influenced by emission from AGN, TP-AGB stars, and strong PAH features (e.g., Alatalo et al. 2017; Smercina et al. 2018). In future studies, we will perform stacking analyses of the WISE imaging for SQuIGGLE galaxies to understand the nature of this excess W4 emission. Additionally, the mid-infrared capabilities of JWST may allow us to understand the origin of this emission. These infrared studies can be paired with studies of the molecular gas reservoirs in order to obtain a more complete picture of the ISM conditions as galaxies cease forming stars.

7. Discussion and Conclusions

In this paper, we present the sample selection, stellar population properties, SFHs, and objectives of the SQuIGGLE survey of post-starburst galaxies. We select bright, intermediate-redshift, recently quenched galaxies from the SDSS spectroscopic sample using a simple color-based selection criterion. Using just two rest-frame color cuts, we are able to

isolate 1318 post-starburst galaxies at $0.5 < z \lesssim 0.9$. These galaxies all have high $H\delta$ equivalent widths, low D_n4000 values, and BV/A-star-dominated spectra indicating young stellar ages. These recently quenched galaxies serve as laboratories to study the processes responsible for shutting down star formation in galaxies: the signatures of the quenching process should still be imprinted on their morphologies, kinematics, and gas properties.

We use the `Prospector` spectral energy distribution fitting code to recover the stellar population parameters and SFHs of all SQuIGGLE galaxies. We find that these galaxies are very massive—nearly all SQuIGGLE galaxies have $M_* > 10^{11} M_\odot$ —and have relatively low dust attenuation values. Our fitting also shows that these galaxies are indeed quenched: the median SFRs recovered from our SED fitting are more than an order of magnitude below the star-forming main sequence (Whitaker et al. 2012b). The quenched nature of this sample is consistent with SFR estimates based on both the $H\beta$ and [O II] spectral lines: while these SFRs are likely less reliable than the SED SFRs due to the competing effects of LINER emission and dust (see also, e.g., Belli et al. 2021), the median $H\beta$ and [O II] SFRs also lie well below the main sequence. Longer-wavelength data would be required to fully rule out the possibility of highly dust-obscured star formation. While many galaxies in SQuIGGLE host obscured (type II) AGN (Greene et al. 2020), because we mask the [O II] and [O III] lines, we do not expect our SED fitting results to be dominated by AGN emission.

Our SED fitting also allows us to quantify the properties of the recent burst. By using nonparametric SFHs, our SED fitting methodology accurately recovers both how long these galaxies have been quenched (t_q) and the fraction of the total stellar mass formed in the recent burst (f_{burst}). We find that SQuIGGLE galaxies quenched their star formation extremely recently, with a median t_q value of just 175 Myr. Galaxies that quenched longer ago, up to ~ 800 Myr before the time of observation, are also included in SQuIGGLE; however, these older post-starburst galaxies are only selected if they also have relatively high burst mass fractions. The f_{burst} distribution of SQuIGGLE galaxies peaks at around $\sim 30\%$ of the total stellar mass being formed in the recent burst. We note that due to our conservative choice of priors, we likely underestimate f_{burst} for the most extreme and burst-dominated objects. Despite this choice, we find that 20% of the galaxies in SQuIGGLE formed a *majority* of their total stellar mass during the recent burst.

We find that these extreme objects are younger and more burst-dominated than samples of “K+A” or “E+A” post-starburst galaxies at $z \sim 0$: SQuIGGLE galaxies have higher median $H\delta$ equivalent width, lower D_n4000 values, and bluer spectral slopes than the French et al. (2015) sample of local post-starburst galaxies. This difference is also confirmed by the SFH fitting in French et al. (2018): many local post-starburst galaxies have burst mass fractions $\lesssim 20\%$, in contrast to the higher burst mass fractions we find for SQuIGGLE galaxies. While SQuIGGLE galaxies may have slightly lower average burst mass fractions than $z \sim 1$ post-starburst galaxies from Wild et al. (2020), SQuIGGLE galaxies are on average younger than the Wild et al. (2020) post-starburst galaxies. Together, these results indicate that our selection was able to identify the rare intermediate-redshift tail of the peak epoch of quenching at $z > 1$: SQuIGGLE galaxies recently and rapidly shut down a major burst of star formation. By targeting these



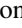
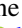

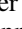
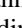
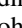


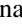


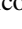
bright, intermediate-redshift galaxies, SQuIGGLE is able to strike a balance between low enough redshifts that follow-up observations are feasible, and high enough redshifts that we can use these galaxies to understand how galaxies shut down their major star-forming epoch.

This large sample of recently quenched galaxies opens a wide range of future studies. Different theoretical quenching mechanisms predict qualitatively different morphologies, age gradients, kinematics, AGN incidence, and ISM conditions. We have already begun to use this sample of galaxies to constrain the mechanisms responsible for quenching. We have found that, in contrast to theoretical predictions, quenching does *not* require the total removal of molecular gas (Suess et al. 2017). Furthermore, we have found that these recently quenched galaxies can have a range of different kinematic structures, but tend to have flat age gradients indicating that the recent starburst was not purely centrally concentrated (Hunt et al. 2018; Setton et al. 2020). We have also shown that AGN likely play an important role in quenching: SQuIGGLE galaxies are more than 10 times more likely to host an optical AGN than a mass-matched sample of older quiescent galaxies, and the AGN fraction is even higher in the youngest SQuIGGLE galaxies (Greene et al. 2020). These studies represent just the beginning of the insights that the SQuIGGLE sample will provide into the mechanisms responsible for transforming galaxies from disk blue star-formers to quiescent red ellipticals.

We thank the anonymous referee for a constructive report which improved the quality of this manuscript. K.A.S. thanks Dustin Lang for kindly providing unWISE fluxes for the SQuIGGLE catalog. R.S.B., J.E.G., D.S., and D.N. gratefully acknowledge support from NSF-AAG#1907697. This work was performed in part at the Aspen Center for Physics, which is supported by National Science Foundation grant PHY-1607611. K.A.S. is partially supported by the UCSC Chancellor’s Fellowship. This publication makes use of data products from the Sloan Digital Sky Survey as well as the Wide-field Infrared Survey Explorer, which is a joint project of the University of California, Los Angeles, and the Jet Propulsion Laboratory/California Institute of Technology, funded by the National Aeronautics and Space Administration. Funding for SDSS-III has been provided by the Alfred P. Sloan Foundation, the Participating Institutions, the National Science Foundation, and the U.S. Department of Energy Office of Science. The SDSS-III website is <http://www.sdss3.org/>. SDSS-III is managed by the Astrophysical Research Consortium for the Participating Institutions of the SDSS-III Collaboration including the University of Arizona, the Brazilian Participation Group, Brookhaven National Laboratory, Carnegie Mellon University, University of Florida, the French Participation Group, the German Participation Group, Harvard University, the Instituto de Astrofísica de Canarias, the Michigan State/Notre Dame/JINA Participation Group, Johns Hopkins University, Lawrence Berkeley National Laboratory, Max Planck Institute for Astrophysics, Max Planck Institute for Extraterrestrial Physics, New Mexico State University, New York University, Ohio State University, Pennsylvania State University, University of Portsmouth, Princeton University, the Spanish Participation Group, University of Tokyo, University of Utah, Vanderbilt University, University of Virginia, University of Washington, and Yale University.

Software: astropy (Astropy Collaboration et al. 2013, 2018),
seaborn (Waskom 2021).

ORCID iDs

Katherine A. Suess  <https://orcid.org/0000-0002-1714-1905>
 Mariska Kriek  <https://orcid.org/0000-0002-7613-9872>
 Rachel Bezanson  <https://orcid.org/0000-0001-5063-8254>
 Jenny E. Greene  <https://orcid.org/0000-0002-5612-3427>
 David Setton  <https://orcid.org/0000-0003-4075-7393>
 Justin S. Spilker  <https://orcid.org/0000-0003-3256-5615>
 Robert Feldmann  <https://orcid.org/0000-0002-1109-1919>
 Andy D. Goulding  <https://orcid.org/0000-0003-4700-663X>
 Benjamin D. Johnson  <https://orcid.org/0000-0002-9280-7594>
 Joel Leja  <https://orcid.org/0000-0001-6755-1315>
 Desika Narayanan  <https://orcid.org/0000-0002-7064-4309>
 Qiana Hunt  <https://orcid.org/0000-0002-4669-0209>
 Sidney Lower  <https://orcid.org/0000-0003-4422-8595>
 Margaret Verrico  <https://orcid.org/0000-0003-1535-4277>

References

- Abolfathi, B., Aguado, D. S., Aguilar, G., et al. 2018, *ApJS*, 235, 42
 Aihara, H., Arimoto, N., Armstrong, R., et al. 2018, *PASJ*, 70, S4
 Akins, H. B., Narayanan, D., Whitaker, K. E., et al. 2021, arXiv:2105.12748
 Alatalo, K., Bitsakis, T., Lanz, L., et al. 2017, *ApJ*, 843, 9
 Alatalo, K., Cales, S. L., Rich, J. A., et al. 2016, *ApJS*, 224, 38
 Alatalo, K., Lacy, M., Lanz, L., et al. 2015, *ApJ*, 798, 31
 Almaini, O., Wild, V., Maltby, D. T., et al. 2017, *MNRAS*, 472, 1401
 Astropy Collaboration, Price-Whelan, A. M., Sipőcz, B. M., et al. 2018, *AJ*, 156, 123
 Astropy Collaboration, Robitaille, T. P., Tollerud, E. J., et al. 2013, *A&A*, 558, A33
 Balogh, M. L., Morris, S. L., Yee, H. K. C., Carlberg, R. G., & Ellingson, E. 1999, *ApJ*, 527, 54
 Barro, G., Faber, S. M., Pérez-González, P. G., et al. 2013, *ApJ*, 765, 104
 Becker, R. H., White, R. L., & Helfand, D. J. 1995, *ApJ*, 450, 559
 Behroozi, P., Wechsler, R. H., Hearin, A. P., & Conroy, C. 2019, *MNRAS*, 488, 3143
 Belli, S., Contursi, A., Genzel, R., et al. 2021, *ApJL*, 909, L11
 Belli, S., Newman, A. B., & Ellis, R. S. 2019, *ApJ*, 874, 17
 Bezanson, R., Spilker, J. S., Suess, K. A., et al. 2022, *ApJ*, 925, 153
 Bezanson, R., van Dokkum, P., van de Sande, J., Franx, M., & Kriek, M. 2013, *ApJL*, 764, L8
 Blanton, M. R., Hogg, D. W., Bahcall, N. A., et al. 2003, *ApJ*, 594, 186
 Brown, M. J. I., Moustakas, J., Caldwell, N., et al. 2009, *ApJ*, 703, 150
 Byler, N., Dalcanton, J. J., Conroy, C., & Johnson, B. D. 2017, *ApJ*, 840, 44
 Calzetti, D., Armus, L., Bohlin, R. C., et al. 2000, *ApJ*, 533, 682
 Cappellari, M. 2017, *MNRAS*, 466, 798
 Cappellari, M., & Emsellem, E. 2004, *PASP*, 116, 138
 Carnall, A. C., Leja, J., Johnson, B. D., et al. 2019, *ApJ*, 873, 44
 Carnall, A. C., McLure, R. J., Dunlop, J. S., & Davé, R. 2018, *MNRAS*, 480, 4379
 Chabrier, G. 2003, *PASP*, 115, 763
 Chan, J. C. C., Beifiori, A., Mendel, J. T., et al. 2016, *MNRAS*, 458, 3181
 Choi, J., Dotter, A., Conroy, C., et al. 2016, *ApJ*, 823, 102
 Conroy, C., & Gunn, J. E. 2010, *ApJ*, 712, 833
 Conroy, C., Gunn, J. E., & White, M. 2009, *ApJ*, 699, 486
 Couch, W. J., & Sharples, R. M. 1987, *MNRAS*, 229, 423
 Davis, T. A., van de Voort, F., Rowlands, K., et al. 2019, *MNRAS*, 484, 2447
 Dawson, K. S., Schlegel, D. J., Ahn, C. P., et al. 2013, *AJ*, 145, 10
 Di Matteo, T., Springel, V., & Hernquist, L. 2005, *Nature*, 433, 604
 Dotter, A. 2016, *ApJS*, 222, 8
 Draine, B. T., & Li, A. 2007, *ApJ*, 657, 810
 Dressler, A., & Gunn, J. E. 1983, *ApJ*, 270, 7
 Dressler, A., Smail, I., Poggianti, B. M., et al. 1999, *ApJS*, 122, 51
 Emsellem, E., Cappellari, M., Krajnović, D., et al. 2011, *MNRAS*, 414, 888
 Evans, I. N., Primi, F. A., Glotfelty, K. J., et al. 2010, *ApJS*, 189, 37
 Faber, S. M., Pérez-González, P. G., et al. 2014, *ApJ*, 791, 52
 Falcón-Barroso, J., Sánchez-Blázquez, P., Vazdekis, A., et al. 2011, *A&A*, 532, A95
 Feldmann, R., Carollo, C. M., & Mayer, L. 2011, *ApJ*, 736, 88
 Forrest, B., Tran, K.-V. H., Broussard, A., et al. 2018, *ApJ*, 863, 131
 French, K. D. 2021, *PASP*, 133, 072001
 French, K. D., Yang, Y., Zabludoff, A., et al. 2015, *ApJ*, 801, 1
 French, K. D., Yang, Y., Zabludoff, A. I., & Tremonti, C. A. 2018, *ApJ*, 862, 2
 Gallazzi, A., Charlot, S., Brinchmann, J., White, S. D. M., & Tremonti, C. A. 2005, *MNRAS*, 362, 41
 Goto, T. 2005, *MNRAS*, 357, 937
 Greene, J. E., Janish, R., Ma, C.-P., et al. 2015, *ApJ*, 807, 11
 Greene, J. E., Setton, D., Bezanson, R., et al. 2020, *ApJL*, 899, L9
 Hickox, R. C., Mullaney, J. R., Alexander, D. M., et al. 2014, *ApJ*, 782, 9
 Hopkins, P. F., Hernquist, L., Cox, T. J., & Dušan, K. 2008, *ApJS*, 175, 356
 Hopkins, P. F., Somerville, R. S., Hernquist, L., et al. 2006, *ApJ*, 652, 864
 Hubble, E. P. 1926, *ApJ*, 64, 321
 Hunt, Q., Bezanson, R., Greene, J. E., et al. 2018, *ApJL*, 860, L18
 Johnson, B., & Leja, J. 2017, Bd-J/Prospector: Initial Release, v0.1, Zenodo, doi:10.5281/zenodo.1116491
 Johnson, B. D., Leja, J., Conroy, C., & Speagle, J. S. 2021, *ApJS*, 254, 22
 Kauffmann, G., Heckman, T. M., White, S. D. M., et al. 2003, *MNRAS*, 341, 54
 Kaviraj, S., Kirkby, L. A., Silk, J., & Sarzi, M. 2007, *MNRAS*, 382, 960
 Kennicutt, Robert C., Jr. 1998a, *ApJ*, 498, 541
 Kennicutt, R. C., Jr. 1998b, *ARA&A*, 36, 189
 Kocevski, D. D., Lemaux, B. C., Lubin, L. M., et al. 2011, *ApJL*, 737, L38
 Kriek, M., & Conroy, C. 2013, *ApJL*, 775, L16
 Kriek, M., Labbé, I., Conroy, C., et al. 2010, *ApJL*, 722, L64
 Lee, S.-K., Ferguson, H. C., Somerville, R. S., Wiklund, T., & Gialalisco, M. 2010, *ApJ*, 725, 1644
 Lee, S.-K., Idzi, R., Ferguson, H. C., et al. 2009, *ApJS*, 184, 100
 Leja, J., Carnall, A. C., Johnson, B. D., Conroy, C., & Speagle, J. S. 2019a, *ApJ*, 876, 3
 Leja, J., Johnson, B. D., Conroy, C., et al. 2019b, *ApJ*, 877, 140
 Leja, J., Johnson, B. D., Conroy, C., van Dokkum, P. G., & Byler, N. 2017, *ApJ*, 837, 170
 Lemaux, B. C., Lubin, L. M., Shapley, A., et al. 2010, *ApJ*, 716, 970
 Lower, S., Narayanan, D., Leja, J., et al. 2020, *ApJ*, 904, 33
 Maddox, N. 2018, *MNRAS*, 480, 5203
 Maltby, D. T., Almaini, O., Wild, V., et al. 2016, *MNRAS*, 459, L114
 Maltby, D. T., Almaini, O., Wild, V., et al. 2018, *MNRAS*, 480, 381
 Maraston, C., Pforr, J., Renzini, A., et al. 2010, *MNRAS*, 407, 830
 Martig, M., Bournaud, F., Teyssier, R., & Dekel, A. 2009, *ApJ*, 707, 250
 Naab, T., Johansson, P. H., & Ostriker, J. P. 2009, *ApJ*, 699, L178
 Noeske, K. G., Weiner, B. J., Faber, S. M., et al. 2007, *ApJL*, 660, L43
 Patarekijwanich, P., Strauss, M. A., Ho, S., & Ross, N. P. 2016, *ApJ*, 833, 19
 Paxton, B., Bildsten, L., Dotter, A., et al. 2011, *ApJS*, 192, 3
 Paxton, B., Cantiello, M., Arras, P., et al. 2013, *ApJS*, 208, 4
 Paxton, B., Marchant, P., Schwab, J., et al. 2015, *ApJS*, 220, 15
 Quintero, A. D., Hogg, D. W., Blanton, M. R., et al. 2004, *ApJ*, 602, 190
 Rowlands, K., Wild, V., Bourne, N., et al. 2018, *MNRAS*, 473, 1168
 Rowlands, K., Wild, V., Nesvadba, N., et al. 2015, *MNRAS*, 448, 258
 Salim, D. M., Alatalo, K., Federrath, C., Groves, B., & Kewley, L. J. 2020, *ApJ*, 893, 26
 Sánchez-Blázquez, P., Peletier, R. F., Jiménez-Vicente, J., et al. 2006, *MNRAS*, 371, 703
 Sazonova, E., Alatalo, K., Rowlands, K., et al. 2021, *ApJ*, 919, 134
 Schawinski, K., Urry, C. M., Simmons, B. D., et al. 2014, *MNRAS*, 440, 889
 Setton, D. J., Bezanson, R., Suess, K. A., et al. 2020, *ApJ*, 905, 79
 Shen, S., Mo, H. J., White, S. D. M., et al. 2003, *MNRAS*, 343, 978
 Smercina, A., Smith, J. D. T., Dale, D. A., et al. 2018, *ApJ*, 855, 51
 Speagle, J. S. 2020, *MNRAS*, 493, 3132
 Springel, V., Di Matteo, T., & Hernquist, L. 2005, *ApJL*, 620, L79
 Suess, K. A., Bezanson, R., Spilker, J. S., et al. 2017, *ApJL*, 846, L14
 Suess, K. A., Kriek, M., Price, S. H., & Barro, G. 2020, *ApJL*, 899, L26
 Suess, K. A., Kriek, M., Price, S. H., & Barro, G. 2021, *ApJ*, 915, 87
 Tacchella, S., Carollo, C. M., Förster Schreiber, N. M., et al. 2018, *ApJ*, 859, 56
 Tacchella, S., Conroy, C., Faber, S. M., et al. 2021, arXiv:2102.12494
 van der Wel, A., Noeske, K., Bezanson, R., et al. 2016, *ApJS*, 223, 29
 Waskom, M. L. 2021, *JOSS*, 6, 3021
 Wellons, S., Torrey, P., Ma, C.-P., et al. 2015, *MNRAS*, 449, 361
 Whitaker, K. E., Kriek, M., van Dokkum, P. G., et al. 2012a, *ApJ*, 745, 179
 Whitaker, K. E., van Dokkum, P. G., Brammer, G., & Franx, M. 2012b, *ApJL*, 754, L29
 Wild, V., Almaini, O., Cirasuolo, M., et al. 2014, *MNRAS*, 440, 1880
 Wild, V., Almaini, O., Dunlop, J., et al. 2016, *MNRAS*, 463, 832
 Wild, V., Taj Aldeen, L., Carnall, A., et al. 2020, *MNRAS*, 494, 529

Williams, C. C., Spilker, J. S., Whitaker, K. E., et al. 2021, [ApJ](#), **908**, 54
Woo, J., & Ellison, S. L. 2019, [MNRAS](#), **487**, 1927
Wu, P.-F., van der Wel, A., Bezanson, R., et al. 2018, [ApJ](#), **868**, 37
Wuyts, S., Förster Schreiber, N. M., Lutz, D., et al. 2011, [ApJ](#), **738**, 106

Yan, R., Newman, J. A., Faber, S. M., et al. 2006, [ApJ](#), **648**, 281
Yano, M., Kriek, M., van der Wel, A., & Whitaker, K. E. 2016, [ApJL](#), **817**, L21
Zabludoff, A. I., Zaritsky, D., Lin, H., et al. 1996, [ApJ](#), **466**, 104